Nano Research

ISSN 1998-0124 CN 11-5974/O4
https://doi.org/10.26599/NR.2026.94908756

Research Article

Interface-stabilized phosphorene/bismuthene heterostructures for freeze-tolerant micro-supercapacitors and integrated sensing

Yukai Chang[1](✉), Chenfang Lou[1], Jin Jia[2], Huilan Zhao[1], Penghui Li[3](✉), Yingjie Huo[4], Libo Wang[1], Qianku Hu[1], Yuanyuan Zhu[2](✉), Aiguo Zhou[1](✉)

[1] School of Materials Science and Engineering, Henan Polytechnic University, Jiaozuo 454003, China

[2] Key Laboratory of Spin Electron and Nanomaterials of Anhui Higher Education Institutes, Suzhou University, Suzhou 234000, China

[3] Center for High Pressure Science (CHiPS), State Key Laboratory of Metastable Materials Science and Technology, Yanshan University, Qinhuangdao 066004, China

[4] School of Physical Science and Technology, Tangshan Normal University, Tangshan 063000, China

Nano Res., **Just Accepted Manuscript** • https://doi.org/10.26599/NR.2026.94908756

https://www.sciopen.com/journal/1998-0124 on Apr. 20, 2026

Just Accepted

Table of

Contents

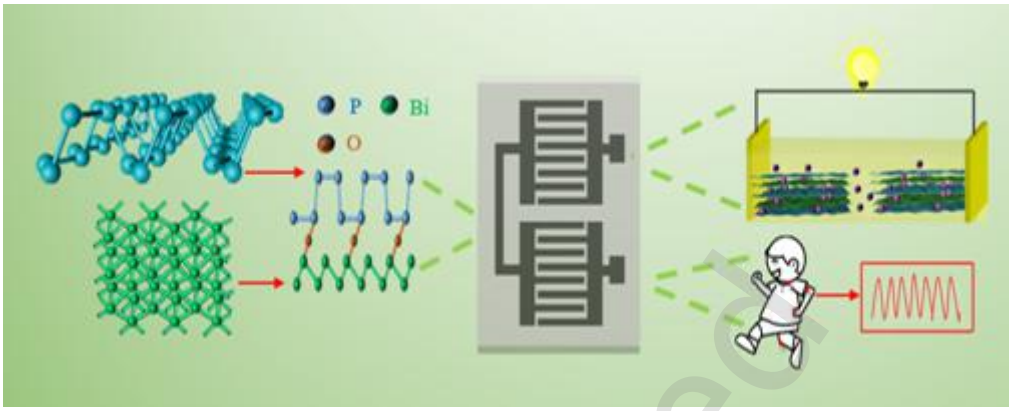

This work constructs a stable BP/Bi heterojunction for freeze-tolerant micro-supercapacitors and demonstrates their integration into a flexible, self-powered sensing system.

Research Article

Interface-stabilized phosphorene/bismuthene heterostructures for freeze-tolerant micro-supercapacitors and integrated sensing

Yukai Chang[1,*], Chenfang Lou[1], Jin Jia[2], Huilan Zhao[1], Penghui Li[3,*], Yingjie Huo[4], Libo Wang[1], Qianku Hu[1], Yuanyuan Zhu[2,*], and Aiguo Zhou[1,*]

[1] School of Materials Science and Engineering, Henan Polytechnic University, Jiaozuo 454003, China

[2] Key Laboratory of Spin Electron and Nanomaterials of Anhui Higher Education Institutes, Suzhou University, Suzhou 234000, China

[3] Center for High Pressure Science (CHiPS), State Key Laboratory of Metastable Materials Science and Technology, Yanshan University, Qinhuangdao 066004, China

[4] School of Physical Science and Technology, Tangshan Normal University, Tangshan 063000, China

Received: 2 March 2026; Revised: 16 April 2026; Accepted: 17 April 2026

*Address correspondence to Yukai Chang, yukaichang12345@hpu.edu.cn; Penghui Li, ysulph@163.com; Yuanyuan Zhu, zhuyy@ahszu.edu.cn; Aiguo Zhou, zhouag@hpu.edu.cn

Cite this article: Nano Research, 2026, 19, 9490875

https://doi.org/10.26599/NR.2026.94908756

Abstract

High-performance black phosphorus (BP)-based micro-supercapacitors (MSCs) hold immense promise for wearable electronics but remain hampered by the material's intrinsic instability and sluggish electron kinetics. Herein, a two-dimensional phosphorene and bismuthene (2D BP/Bi) heterojunction via liquid nitrogen-assisted exfoliation and mask-assisted filtration was developed as a robust bifunctional electrode for integrated flexible energy-sensing systems. The heterostructure effectively suppresses nanosheet restacking and enhances interfacial stability through strong P-O-Bi covalent bonding and interfacial synergy. Simultaneously, the incorporation of bismuthene constructs high-speed electron transport channels, significantly facilitating ion diffusion and charge transfer. Consequently, the optimized electrode achieved a high areal capacitance of 7.6 mF cm^{-2} (1.6-fold enhancement over pure BP) and an ultra-long lifespan with 92.1% retention after 30,000 cycles. Notably, by tailoring the gel electrolyte with DMSO, the device exhibited remarkable freeze-tolerance, maintaining 70% capacitance at -35 °C. Furthermore, an all-flexible integrated system combining the MSC with a pressure sensor was constructed using graphene current collectors, enabling continuous, self-sustained physiological monitoring. This work offers critical insights into interface engineering for designing high-performance BP-based MSCs and paves the way for extreme-environment wearable applications.

Key words: Micro-supercapacitor; Phosphorene/bismuthene; Interface engineering; Integrated sensing; Flexible electronics

1. Introduction

With the rapid advancement of the Internet of Things (IoT), artificial intelligence (AI), and flexible electronic technologies, wearable devices are increasingly penetrating critical applications such as real-time health monitoring[1], human-machine interaction, and precision motion tracking[2]. However, conventional wearable systems rely on discrete functional modules (separate power sources, sensors, and connectors), leading to bulky configurations, poor mechanical conformability, and performance degradation under dynamic deformation (bending, stretching). These critical bottlenecks hinder their integration into complex human-centric scenarios. Thus, the development of next-generation lightweight, miniaturized, and multifunctional wearable electronics urgently demands integrated energy storage-sensing modules with high performance, long-term stability, and extreme environmental adaptability[3–5]. In recent years, planar micro-supercapacitors (MSCs) have emerged as promising micro-scale energy storage solutions. These devices not only inherit the advantages of conventional supercapacitors but also exhibit excellent mechanical flexibility, enhanced safety[6], considerable potential for miniaturization and system integration owing to their distinctive planar configurations. These attributes make them particularly suitable for microelectronic devices, wearable systems, and IoT applications, positioning MSCs as the ideal energy storage components for next-generation integrated flexible wearable electronic systems[7]. This necessitates the development of dual-function electrode materials that synergistically fulfill high-energy-density requirements for MSCs while

enabling sensing functionalities.

Two-dimensional black phosphorus (2D BP), a star material in advanced energy storage, has attracted widespread attention due to its unique corrugated structure and excellent physicochemical properties, demonstrating broad application potential in electrochemical energy storage systems[8]. With a high theoretical specific capacity of 2596 mAh g^{-1}, phosphorene is regarded as a promising anode material for lithium-ion batteries (LIBs). Nevertheless, their practical deployment in secondary batteries is severely hampered by substantial volume expansion (~490%) during lithiation/delithiation[9]. In contrast, BP exhibits promising performance in supercapacitors, where its double-layer charge storage mechanism avoids significant structural changes[10].

In 2016, Hao et al.[11] applied phosphorene to flexible solid-state supercapacitors with a sandwich structure, achieving a volumetric specific capacitance of 13.75 F cm^{-3} (45.8 F g^{-1}) at 0.01 V s^{-1}, demonstrating its potential in supercapacitor applications. Nevertheless, the device exhibited only 84.5% capacitance retention after 10,000 cycles, primarily due to the inherently low electrical conductivity of BP (300 S m^{-1}), which severely limits ion diffusion and charge transfer kinetics. To address this limitation, Wu et al.[12] developed a BP-carbon nanotube heterostructure via microfluidic spinning, introduced a porous architecture that enhanced electrical conductivity, cycle stability, and mechanical robustness (volumetric capacitance: 308.7 F cm^{-3}, 90.2% retention after 10,000 cycles). However, these investigations were confined to conventional three-dimensional sandwich-structured supercapacitors,

suffering from excessive device thickness, limited mechanical flexibility, and poor scalability for system integration. To overcome these issues, Wu's team[13] fabricated interdigitated planar MSCs via layer-by-layer vacuum filtration, integrating phosphorene with graphene. Using an ionic liquid electrolyte, the device achieved a 3 V operating voltage window and 9.8 mF cm^{-2} areal capacitance. Nevertheless, long-term cycling stability was insufficiently explored (only 89.5% retention after 2,000 cycles) and ionic liquid electrolytes suffered from high cost, low ionic mobility, and inferior low-temperature performance. Therefore, the development of high-energy-density, anti-freezing, and long-cycle-life MSCs with dual-function electrode materials remains a pressing challenge.

Beyond energy storage, phosphorene is a promising candidate for next-generation high-sensitivity sensors, attributed to its layer-dependent tunable bandgap (0.3-2.0 eV), high charge-carrier mobility (~1000 $cm^2 V^{-1} s^{-1}$)[14], strong surface activity[15], and inherent mechanical flexibility[16]. BP-based gas sensors (FET and chemiresistive types) leverage electronic anisotropy and conductivity changes upon gas adsorption[17], with monolayer phosphorene showing enhanced binding energy and current responses to nitrogen oxides (NO, NO_2) compared to CO, CO_2, and NH_3[18–21]. For biological sensing, surface-functionalized BP enables detection of proteins, RNAs, and tumor cells[22,23]. Notably, the mechanical flexibility and anisotropy of phosphorene render it suitable for pressure/strain sensing[24–26]. For example, Chen et al.[27] fabricated a BP-based flexible pressure sensor with high sensitivity (0-100 kPa) and rapid response to physiological activities. However,

single-function sensors can no longer meet the growing demands of intelligent wearable electronics. Zhang et al.[28] reported a BP/MXene composite-based integrated system (pressure sensor supercapacitor) via layer-by-layer self-assembly, but this design relied on external circuit connections, leading to poor miniaturization, flexibility, and system-level integration - limitations that persist in recent studies. Given the extensive research on phosphorene in both energy storage and sensors, the development and design of BP-based dual-function electrode materials that enable seamless, wire-free integration of MSCs and sensors is critical for advancing integrated flexible wearable systems.

In this work, a 2D BP/Bi heterojunction was developed as a dual-function electrode material for integrated flexible MSCs and pressure sensors. To address intrinsic instability and low conductivity of BP, liquid nitrogen-assisted low-energy liquid-phase exfoliation was employed to efficiently produce few-layer phosphorene and bismuthene, constructing a heterostructure that synergistically enhances electron transfer efficiency and structural stability. Using mask-assisted vacuum filtration, integrated devices without current collectors were fabricated, eliminating the need for external circuit connections. When the BP/Bi composite ratio is 3:1, the heterojunction exhibits a high areal capacitance of 7.6 mF cm^{-2} (1.6 times that of pure BP) and superior long-term stability (92.1% capacitance retention after 30,000 cycles), outperforming single-component materials. Moreover, with the DMSO-modified organohydrogel electrolyte, the MSC exhibits 70% capacitance retention at -35 °C, demonstrating outstanding anti-freezing characteristics for extreme low-temperature

environments. More importantly, the BP-based MSC is wirelessly integrated with a pressure sensor on a flexible substrate, enabling continuous monitoring of human physiological movements with high sensitivity and rapid response. This work not only provides a novel strategy for designing high-performance BP-based MSCs but also opens a new avenue for utilizing BP-based dual-function electrodes in integrated flexible wearable systems.

2. Experimental Section

2.1. Materials

Red phosphorus (98.5%, Macklin), Black phosphorus (BP), N-methylpyrrolidone (NMP, 99%, Innochem), bismuth (99.999%, Innochem), ammonium persulfate ($(NH_4)_2S_2O_8$, 98%, Kermel), sulfuric acid (H_2SO_4, 98%, Aladdin), flake graphite (50 mesh), polyvinyl alcohol (PVA, 99%, Aladdin), phosphoric acid (H_3PO_4, 85%, Aladdin), Ethylene glycol (EG, Luoyang), dimethyl sulfoxide (DMSO, 99.5%, Kermel). All chemicals were used as received without further purification unless otherwise specified.

2.2 Preparation of few-layer phosphorene and bismuthene

BP crystals were synthesized from red phosphorus using a high-temperature and high-pressure directional growth technique at 1 GPa and 900 °C for 10 min. Subsequently, 80 mg of the resulting BP powder was dispersed in 80 mL of NMP via wet grinding to form a uniform dispersion (1 mg mL^{-1}). This dispersion was rapidly frozen in liquid nitrogen for 10 min to form solid ice, followed by ultrasonication for 5 - 10 min until complete melting. The freeze-thaw-sonication cycle was repeated 5

times to enhance layer exfoliation. The mixture was further exfoliated via continuous ultrasonication (150 W, 3 h) using an ultrasonic cell disruptor, then centrifuged at 2000 rpm for 20 min to remove unexfoliated bulk particles. The supernatant (0.3 mg mL^{-1}) was collected as stable few-layer phosphorene. Few-layer bismuthene were prepared via the identical procedure, yielding a stable dispersion (0.6 mg mL^{-1}).

2.3 Preparation of graphene

10 g of $(NH_4)_2S_2O_8$ was dissolved in 30 mL of H_2SO_4 (98%) under magnetic stirring for 10 min to homogeneous oxidizing solution. 0.5 g of flake graphite (50 mesh) was gradually added to the solution with stirring for 10 min to ensure uniform mixing. The beaker was sealed with parafilm and incubated at room temperature for 6 h to enable complete intercalation and expansion of graphite layers. The product was washed repeatedly via centrifugation until the supernatant reached pH 7.0, yielding expanded graphite. The expanded graphite was redispersed in deionized water to a concentration of 1 mg mL^{-1}, then subjected to ultrasonication (1 h) using an ultrasonic cell disruptor to obtain a ready-to-use graphene dispersion.

2.4 Preparation of PVA/H_3PO_4 electrolyte

3 g of PVA was accurately weighed and added to 30 mL deionized water. The beaker was then placed in an 85 °C water bath, and the mixture was stirred continuously at 400 rpm for 2 h until PVA was completely dissolved, forming a clear transparent solution. 10 mL of H_3PO_4 (85%) was slowly added dropwise to the PVA solution under constant stirring for 30 min to ensure homogeneous dispersion and complete interaction of H_3PO_4 with PVA. The solution was cooled to room

temperature to form a uniform, transparent, viscous PVA/H_3PO_4 gel electrolyte. For the anti-freezing modified electrolyte, deionized water was replaced with a DMSO/deionized water mixture (volume ratio 1:24), while all other procedures remained identical. PVA/H_3PO_4 gel electrolyte is used for the micro-supercapacitor to provide high ionic conductivity and structural integrity, ensuring low charge transfer resistance and high rate performance.

2.5 Preparation of PVA/EG organohydrogel

EG and deionized water were mixed at a weight ratio of 1:1 under stirring until a homogeneous solvent was formed. PVA was added to the solvent at a concentration of 15 wt% (relative to the total mass of the solvent), the mixture was heated at 90 °C under continuous stirring for 3 h to ensure complete dissolution. The solution was cooled to 70 °C and allowed to stand to eliminate entrapped bubbles. The gel precursor was then subjected to two freeze-thaw cycles, each consisting of freezing at -15 °C for 12 h and thawing at 25 °C for 2 h. Ultimately, a PVA/EG organohydrogel was obtained. PVA/EG is used for the pressure sensor to enable mechanical deformation sensitivity, converting external pressure into electrical signals with excellent stability under repeated cycles.

2.6 Assembly of BP/Bi planar MSCs and integrated sensing system

3 mg of graphene was dispersed in 30 mL of anhydrous ethanol (0.1 mg mL^{-1}) and sonicated for 3 h to obtain a uniform dispersion. Subsequently, using the mask-assisted filtration method, 0.4 mg of graphene and 0.4 mg of BP/Bi mixed solution (with mass ratios of 5:1, 3:1, 1:1, and 1:3) were jointly loaded onto the filter

membrane to form a composite electrode. After the electrode preparation was completed, an appropriate amount of silver paste was evenly coated on the end electrode areas of the MSC, the conductive copper foil was adhered and fixed as the current collector, and then the device was encapsulated and fixed on the glass substrate using inert Kapton tape. Afterwards, PVA/H_3PO_4 gel electrolyte was dropped onto the electrode area to ensure complete coverage of the active materials. For the integrated capacitance-sensing device, a second electrode was fabricated following the same procedure, with the only modification being the replacement of the electrolyte with PVA/EG organohydrogel. A detailed photograph showing the complete integrated system with labeled components (BP/Bi electrodes, copper tape connections, Kapton encapsulation, and electrolyte regions) have been included in Fig. S1.

2.7 Material Characterization

Crystal structures were analyzed using an X-ray diffractometer (XRD, Smart-Lab, Rigaku) with Cu-Kα radiation (λ = 1.5406 A). The microstructure and composition of the material were observed and analyzed using a scanning electron microscope (SEM, Merlin Compact, Zeiss) and its accompanying energy spectrometer (EDS, Oxford FPD), as well as a transmission electron microscope (TEM, JEM-ARM200F, JEOL). Raman spectroscopy was performed on an in via spectrometer with a laser wavelength of 532 nm. Additionally, the elemental composition and chemical state of the sample were characterized using X-ray photoelectron spectroscopy (XPS, ESCALAB 250Xi, Thermo Scientific).

2.8 Electrochemical Measurements

Electrochemical performance was tested using a CHI760E electrochemical workstation (Chenhua Instruments), including cyclic voltammetry (CV), galvanostatic charge-discharge (GCD), and electrochemical impedance spectroscopy (EIS, frequency range 0.01 Hz - 100 kHz). Long-term cycling stability was conducted on a Land battery testing system (LANHE CT3002A). The areal capacitance (C_A), energy density (E), and power density (P) were calculated using the following formulas：

$$C_A = \frac{\int \mathrm{i(V)dV}}{2\mathrm{A}\nu\Delta\mathrm{V}} \#(1)$$

$$\mathrm{E} = \frac{1}{2} C_A (\Delta\mathrm{V})^2 \frac{1}{3600} \#(2)$$

$$\mathrm{P} = \frac{\mathrm{E}}{\Delta\mathrm{t}} \times 3600 \#(3)$$

Here, i (V) represents the response current (A), A (cm^2) is the total area of the two interdigitated active electrode materials, ν is the potential scanning rate (V s^{-1}), ΔV (V) is the stable operating voltage range, fixed at 1 V during charging/discharging, Δt (s) is the galvanostatic discharge time, C_A (F cm^{-2}) is the areal capacitance, E (W h cm^{-2}) and P (W cm^{-2}) are the areal energy density and power density, respectively.

3. Results and Discussion

Phosphorene and bismuthene were synthesized via a liquid nitrogen-assisted liquid-phase exfoliation method[29,30], which achieves a breakthrough in exfoliation efficiency by reducing the total processing time from 10 h to 3 h. The reduced processing time not only enhances exfoliation efficiency but also minimizes surface oxidation and structural damage to the black phosphorus nanosheets.This

improvement stems from the freeze-thaw cycles, ice crystals formed in NMP undergo volume expansion to generate localized mechanical stress during freezing, which efficiently cleaves the weak interlayer van der Waals forces in bulk layered materials. The integrated MSC-sensor device was constructed through a mask-assisted filtration (Fig. S1) process (Fig. 1). The design adopts a layer-by-layer hierarchical architecture to address the trade-off between flexibility, conductivity, and integration capability in conventional wearable systems. First, the bottom layer is composed of vacuum-filtered graphene, serving as a current collector that combines high electrical conductivity and mechanical flexibility. Then, the upper active layer is a BP/Bi composite prepared via ultrasonic mixing and sequential filtration, which synergistically integrates the high theoretical capacitance of BP and the excellent electrical conductivity of Bi to accelerate charge transfer and ion diffusion. Finally, by applying PVA/H_3PO_4 gel electrolyte to the MSC and PVA/EG gel electrolyte to the pressure sensor, an integrated system was achieved for intelligent monitoring applications.

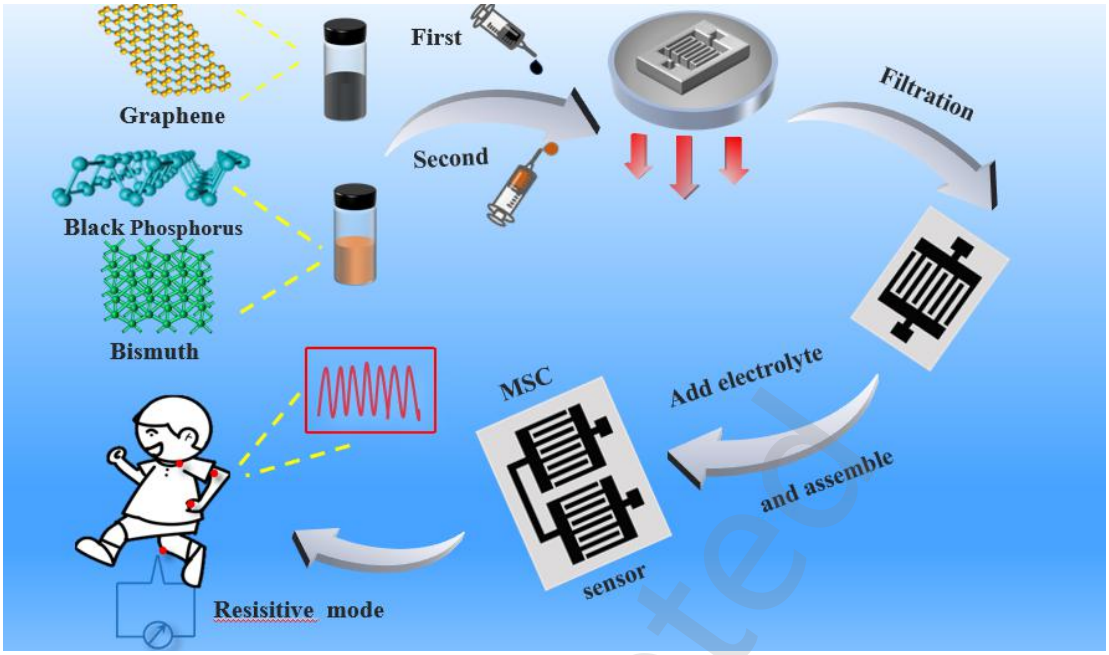

Fig. 1. Mask-assisted simplified fabrication and integration of pressure sensing system for BP/Bi MSC.

The composition, morphology, and surface chemical state of the samples were further analyzed to verify the successful preparation of phosphorene, bismuthene, and 2D BP/Bi heterojunctions. Scanning electron microscopy (SEM) and energy-dispersive X-ray spectroscopy (EDS) analysis of bulk BP and Bi powders revealed distinct layered structures with uniform elemental distribution (Fig. S3). The XRD patterns of both bulk black phosphorus and Bi powder (Fig. S4) confirm high crystallinity without detectable impurities. For the self-assembled freestanding films (Fig. 2a), the XRD pattern of BP nanosheet film exhibited three sharp characteristic peaks at 17.01°, 34.29°, and 52.43° corresponding to the (020), (040), and (060) crystal planes (PDE#74-1878), respectively[31]. This indicates highly oriented in-plane arrangement of phosphorene, attributable to the improved exfoliation technique and the filtration-driven self-assembly. The Bi nanosheet film exhibited two

distinct characteristic peaks at 26.98° and 38.22°, corresponding to the (012) and (110) crystal planes (PDF#85-1229), respectively[32]. Furthermore, the XRD pattern of the BP/Bi heterostructure film clearly integrates all characteristic diffraction peaks of both components, directly demonstrating the formation of 2D BP/Bi heterojunction.

Further Raman spectroscopy (Fig. 2b) provides insights into interfacial interactions. The pure BP spectrum exhibits three typical vibrational modes: A^1_g (361.7 cm^{-1}, in-plane), B^2_g (437.6 cm^{-1}, in-plane), and A^2_g (466.2 cm^{-1}, out-of-plane), while pure Bi shows two characteristic peaks at 70.1 (in-plane E_g) and 95.8 cm^{-1} (out-of-plane A^1_g)[33], respectively. For the BP/Bi heterojunction, all characteristic peaks of BP and Bi are preserved. The locally magnified Raman spectra (Fig. S5) reveal a distinct leftward shift of 361.7 cm^{-1} ,437.6 cm^{-1} and 466.2 cm^{-1} compared to pure BP components. This redshift is attributed to the formation of covalent interfacial bonds, which modulates the electron cloud density of BP and Bi, reducing the force constant of atomic vibrations. X-ray photoelectron spectroscopy (XPS) was employed to clarify surface chemical states and interfacial bonding (Fig. 2c-d, Fig. S4). The survey spectrum confirms the predominant presence of P (35.84%), Bi (3.37.%), and O (60.79%), with no other impurities (Fig. S6). The high-resolution P2p spectrum can be deconvoluted into three peaks: 129.17 eV (P $2p_{3/2}$, metallic P), 130.03 eV (P $2p_{1/2}$, metallic P), and 132.59 eV (P-O, P_xO_y)[34]. The weaker P_xO_y peak may be due to the mild oxidation of phosphorene surface forming P-O or P=O[35]. The high-resolution Bi 4f spectrum shows four peaks (Fig. 2d): 161.57 eV (Bi $4f_{5/2}$, metallic Bi^0), 156.17 eV (Bi $4f_{7/2}$, metallic Bi^0), 163.77 eV (Bi $4f_{5/2}$, Bi^{3+}), and 158.51 eV (Bi $4f_{7/2}$,

Bi^{3+})[36]. The Bi^{3+} content originates from the formation of Bi-O bonds, induced by oxygen-containing groups on BP's surface[33]. Critically, the O 1s spectrum (Fig. S6) can be fitted into three components: 532.97 eV (P-O), 530.2 eV (Bi-O), and 530.97 eV (P-O-Bi interfacial bonds)[37,38], with the P-O-Bi peak accounting for 35% of the total O signal evidence consistent with oxygen-bridged interfacial interaction and strong coupling. In addition, the FTIR spectrum (Fig. S7) shows that the band at 1047.32 cm^{-1} can be assigned to P-O stretching[39], while the peak at 622.93 cm^{-1} corresponds to Bi-O vibration[40]. The coexistence of these P-O and Bi-O features is consistent with the formation of an oxygen-bridged interfacial interaction between BP and Bi. Therefore, the Raman, XPS, and newly added FTIR results collectively support the existence of strong interfacial coupling with oxygen-bridged P-O-Bi bonding. The P-O-Bi bonds not only stabilize BP's crystal structure but also construct an efficient charge transport channel for 2D BP/Bi heterojunction[41].

Transmission electron microscopy (TEM) was used to visualize the microscopic morphology and interfacial structure of the BP/Bi heterojunction (Fig. 2e-l). The low-magnification TEM image (Fig. 2e) shows phosphorene with a lateral size of 400 ± 50 nm and bismuthene with a lateral size of 20 ± 5 nm, with Bi preferentially distributed at the edges of phosphorene. This oriented assembly is attributed to the higher reactivity of BP's edge sites[42], which are prone to oxidation and formation of P-O groups[43]; Bi atoms exhibit strong affinity for oxygen[44], leading to the formation of P-O-Bi covalent bonds at BP's edges and driving oriented nucleation of Bi nanosheets. The high-magnification TEM image (Fig. 2f) and HRTEM images (Fig.

2g) reveal a clear interface between BP and Bi with no obvious lattice distortion. For BP, the measured lattice spacings are 0.234 (020) and 0.326 nm (012)[45], with its selected area electron diffraction (SAED) pattern (Fig. 2h) showing sharp spots indexed to the [00$\bar{1}$] zone axis, verifying single-crystalline BP and oriented alignment. For bismuthene, the lattice spacing of 0.33 nm matches the (012) plane of Bi (Fig. 2g)[37], and its diffuse ring-like SAED (Fig. 2i) reflects mild shear-induced polycrystallinity during the exfoliation. The high-angle annular dark field (HAADF) image and EDS mapping of BP/Bi heterojunction clearly show that P element occupies the main body, while Bi element is mainly concentrated at BP edges (Fig. 2j-l), directly validating edge-selective Bi assembly driven by interfacial P-O-Bi covalent bonding.

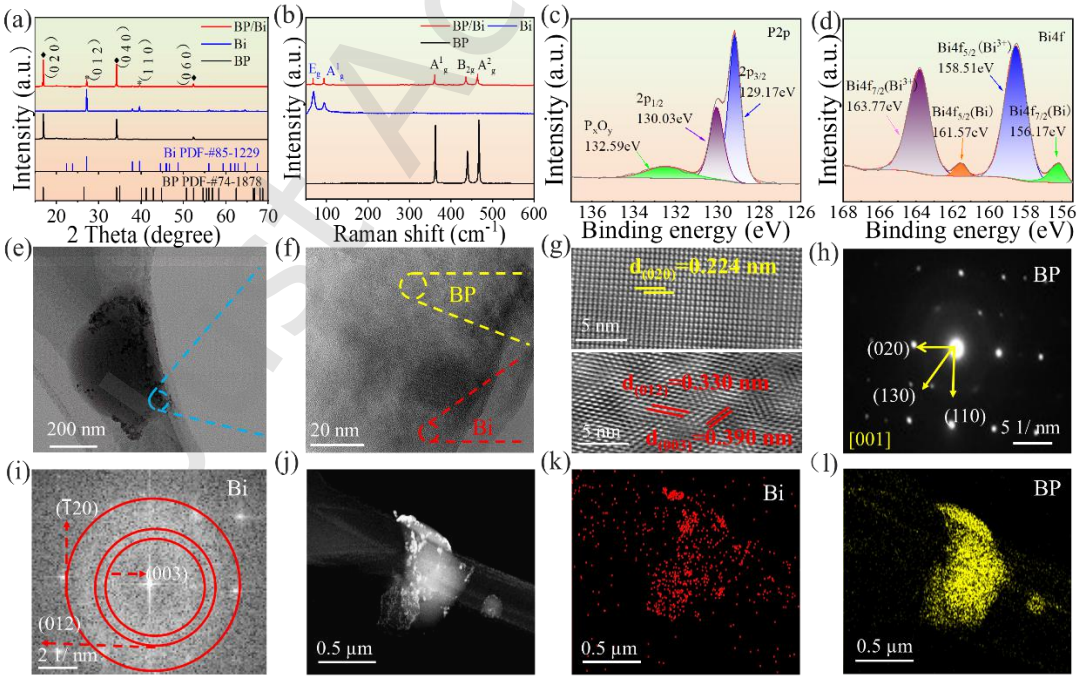

Fig. 2. Characterization of phosphorene, bismuthene, and 2D BP/Bi heterojuncti ons. (a) XRD patterns and (b) Raman spectra of phosphorene, bismuthene and

2D BP/Bi heterojunctions, XPS spectra of (c) phosphorene and (d) bismuthene, (e) TEM image and (f) magnified view of the 2D BP/Bi heterojunction, (g) h igh-resolution TEM image of heterojunction interfacial BP (yellow) and Bi (red) regions, the corresponding SAED pattern of (h) BP and (i) Bi, (j-l) HAADF i mage and the corresponding EDS mapping of 2D BP/Bi heterojunction.

The BP/Bi interdigitated electrode features eight interdigitated fingers with 1 mm width and 1 mm inter-finger spacing (Fig. 3a). EDS mapping of both the surface and cross-section (Fig. 3a, b) confirms uniform P/Bi distribution, indicating good homogeneity and densification of the composite electrode. For the BP/Bi composite with optimized mass ratio of 3:1, cross-sectional SEM images reveal a uniform thickness of approximately 8.9 μm (Fig. 3b).To optimize the composite ratio, MSCs with pure BP, pure Bi, and BP/Bi (1:1, 1:3, 3:1, and 5:1) were fabricated. All samples exhibit quasi-rectangular CV curves and triangular GCD waveforms (Fig. S8-S12), confirming double-layer capacitance. The BP/Bi (3:1) MSC shows the largest CV area (41% larger than pure BP) at 100 mV s^{-1} (Fig. 3c) and longest GCD discharge time (8.4 s) at 0.1 mA cm^{-2} (Fig. 3d)), verifying the 3:1 ratio as optimal. Electrochemical impedance spectroscopy (EIS, Fig. 3e) shows the BP/Bi (3:1) electrode has an equivalent series resistance of 45 (between pure BP (50 Ω) and pure Bi (31 Ω)), attributed to Bi's high conductivity (4.6×10^4 S cm^{-1})[46] and P-O-Bi covalent bonds reducing contact resistance, which facilitate charge transfer across the heterointerface[41]. The BP/Bi (3:1) MSC achieved a peak areal capacitance of 7.46 mF cm^{-2}, representing a 1.6 and 3.5-fold enhancement over pure BP (4.54 mF cm^{-2})

and pure Bi (2.16 mF cm^{-2}), respectively (Fig. 3f). However, further increasing the BP content to 5:1 led to a performance decline, particularly at high scan rates, due to insufficient Bi content, Bi-induced P-O-Bi bonds, and consequent reduction in overall electrical conductivity. As clearly shown in Fig. 3f, the BP/Bi (3:1) MSC exhibits significantly enhanced rate performance, which can be attributed to the synergistic effect of heterojunction construction and the introduction of bismuth. First, the formation of a heterojunction effectively suppresses the self-stacking tendency of black phosphorus nanosheets, maintaining a well-exposed active surface and facilitating ion transport. Second, bismuth, with its high intrinsic conductivity, improves the overall electrical conductivity of the composite. Furthermore, as previously identified, P-O-Bi bonds formed at the heterojunction interface play a crucial role in facilitating interfacial charge transfer. Together, these factors contribute to reduced charge transfer resistance and enhanced rate capability.

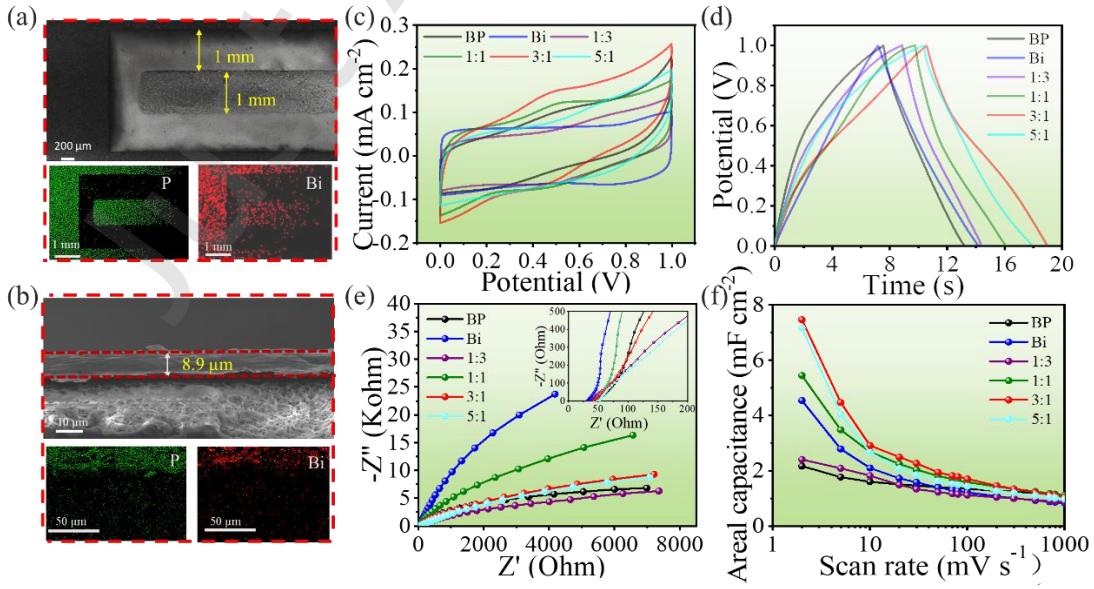

Fig. 3. Characterization and electrochemical performance of BP/Bi interdigitated

electrode films. (a) Surface and (b) cross-sectional SEM/EDS mapping of P/Bi 3:1. Electrochemical performance comparison of different BP/Bi composite rati os (1:1, 1:3, 3:1, and 5:1): (c) CV curves at 100 mV s^{-1}, (d) GCD profiles at 0.1 mA cm^{-2}, (e) EIS, (f) areal capacitance at different scan rates.

The electrochemical performance of the optimized BP/Bi (3:1) electrode was further investigated in detail (Fig. 4). Cyclic voltammetry (CV) curves (0 - 1 V, Fig. 4a-c) show highly symmetric quasi-rectangular profiles at 5 - 10,000 mV s^{-1} (no redox peaks), confirming dominant electric double-layer capacitance (EDLC). The GCD profiles at c 0.07 - 0.11 mA cm^{-2} exhibit symmetric triangular profiles (Fig. 4d), validating ideal EDLC and low internal resistance. Fig. 4e presents areal/gravimetric capacitances: 7.46 mF cm^{-2} (18.52 F g^{-1}) at 2 mV s^{-1}, retaining 1.04 mF cm^{-2} at 1000 mV s^{-1}, outperforming most reported graphene-based MSCs [47]. The Ragone plot in Fig. (4f) shows a maximum 1.03 mWh cm^{-2} and 0.17 mW cm^{-2}, competitive with state-of-the-art MSCs[48–58]. Furthermore, long-term cycling stability was evaluated at 0.1 mA cm^{-2} (Fig. 4g and Fig. S14). Remarkably, the BP/Bi (3:1) MSC exhibited 92.1% of initial capacitance with 91.5% Coulombic efficiency after 30,000 cycles, significantly outperforming pure BP (85.7% capacitance retention, 85.4% efficiency) and pure Bi (80.7% capacitance retention, 80.2% efficiency) MSCs. This enhancement stems from P-O-Bi interfacial bonds that suppress BP oxidation, mitigate structural agglomeration, and stabilize the electrode-electrolyte interface, addressing BP's intrinsic environmental/electrochemical instability. Post-cycling CV/EIS analyses (Fig. S13) indicate minor capacity fade arises from modest increases

in charge transfer resistance (ΔR_{ct} = 48 Ω) and reduced ion diffusion kinetics, which are far less severe than pure BP (ΔR_{ct} = 50 Ω) due to Bi's conductive network maintaining structural integrity. As summarized in Table S1, the BP/Bi (3:1) MSC exhibits superior cycling stability compared to recently reported MSCs (for instance, WS_2: 82% retention after 10,000 cycles; BP: 71.8% after 30,000 cycles; SnP_3/CNT: 88% after 20,000 cycles)[51, 12, 52], highlighting its potential for practical wearable electronics.

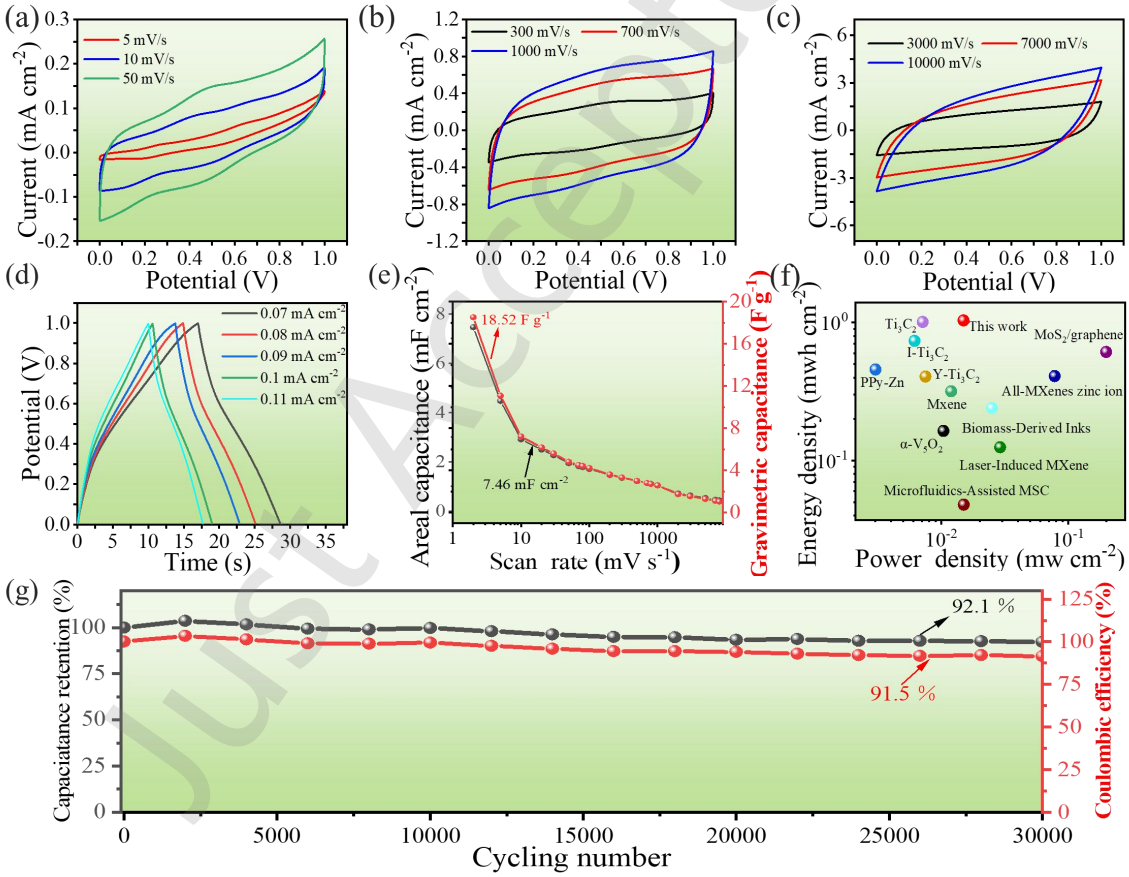

Fig. 4. Electrochemical characterization of BP/Bi (3:1) MSC: (a-c) CV curves at 5-10000 mV s^{-1}, (d) GCD profiles at 0.07 - 0.11 mA cm^{-2}, (e) area/volume capacitances at different scan rates, (f) Ragone plots (energy density vs. power density), (g) cycling stability (30,000 cycles) and Coulombic efficiency.

The flexibility of the BP/Bi (3:1) MSCs was systematically evaluated by bending the device to 0° - 180° and conducting CV tests at 500 mV s^{-1} (Fig. 5a-b). The CV curves maintained high symmetry and no peak distortion/shift under all bending states, confirming mechanical robustness. Even at 180° (maximum deformation), the device maintains 96.0% capacitance retention. Temperature adaptability was assessed over -30 °C to 25 °C (Fig. 5c-e). CV curves at 100 mV s^{-1} retain quasi-rectangular profiles even at -30 °C (Fig. 5c). EIS analysis (Fig. 5d) reveals an anomalous phenomenon: the low-frequency slope becomes steeper with decreasing temperature[59], corresponding to Warburg impedance decreasing from 104 (25 °C) to 193 Ω (-30 °C). This is attributed to BP/Bi heterointerface low-temperature-induced structural reconstruction and suppressed side reactions, which lower interfacial polarization resistance and facilitate ion transport[60,61]. The improved low-temperature performance is primarily due to the DMSO- modified gel electrolyte, which suppresses solvent crystallization and maintains ionic mobility. The BP/Bi heterojunction plays a supporting role by preserving electrode structural integrity and charge- transfer pathways. Thus, the anti- freezing capability is electrolyte- driven, with the heterojunction contributing secondarily to electrochemical stability under subzero conditions[62,63]. Notably, the device retained approximately 70% of its initial capacitance at -30 °C, highlighting its exceptional cryogenic performance. These results confirm the outstanding structural stability and electrochemical reliability of the BP/Bi (3:1) MSC over a wide temperature range, supporting its potential use in low-temperature applications such as polar environments,

high-altitude exploration, and specialized instrumentation.

To demonstrate scalability, multiple BP/Bi (3:1) MSCs were connected in series, expanding the output voltage from 1 V to 2 V (Fig. 5f). The series configuration exhibited CV curves with negligible distortion (500 mV s^{-1}) and GCD profiles with consistent charge-discharge durations (0.2 mA cm^{-2}, Fig. 5g), confirming electrochemical consistency and structural uniformity. Practically, two serially connected devices successfully powered a 2 V LED (Fig. 5h), visually affirming sufficient voltage and energy for small-scale electronics.

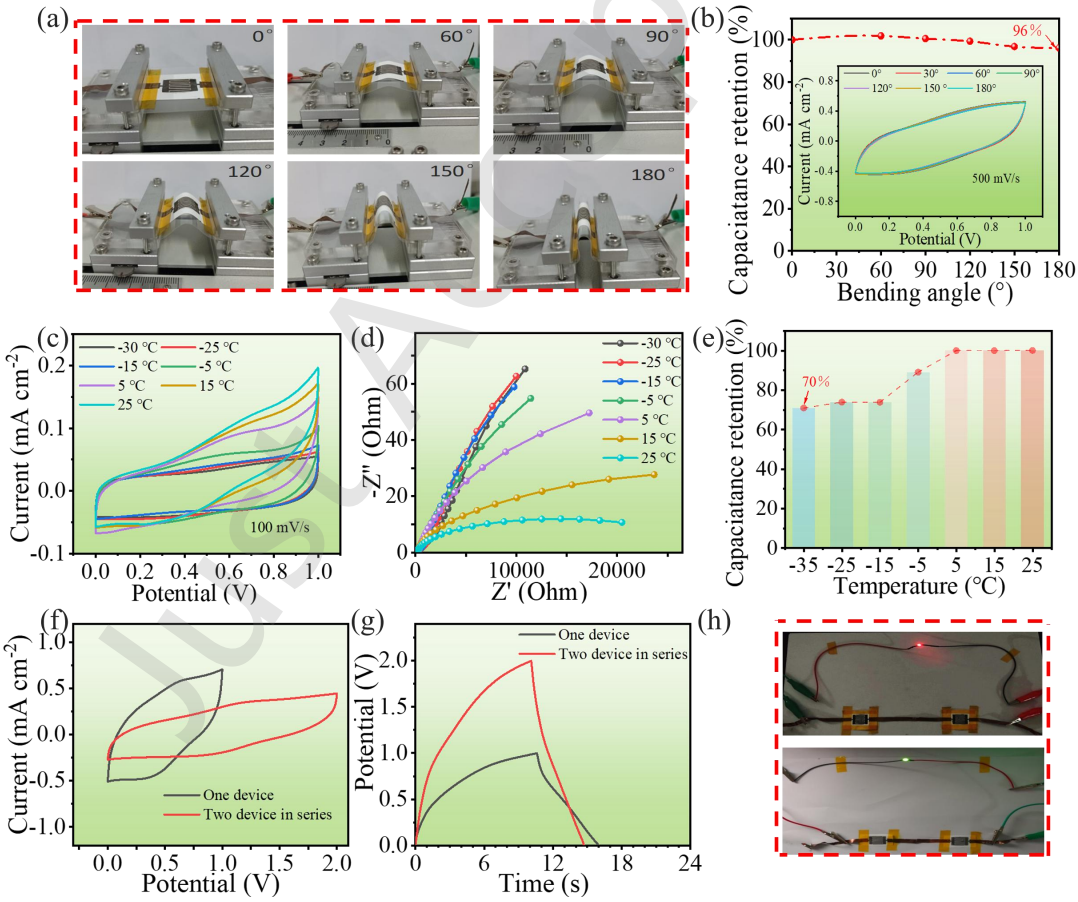

Fig. 5. Flexibility, temperature resilience, and integration of BP/Bi MSCs. (a) Photographs of the MSC under different bending states. (b) Capacitance retention and corresponding CV curves (inset) at 500 mV s^{-1} under various bending conditions.

Electrochemical performance of (c) CV curves at 100 mV s^{-1}, (d) Nyquist plots and (e) Capacity retention rate at -30 ℃ to 25 ℃. (f) CV curves (500 mV s^{-1}) and (g) GCD profiles (0.2 mA cm^{-2}) of serially connected devices. (h) Demonstration of powering a 2 V red and green LEDs.

To address energy storage-sensing integration demands for wearable devices, we developed a monolithic BP/Bi (3:1) system integrating MSC energy storage and piezoresistive sensing, leveraging the synergistic piezoresistive effect of BP/Bi heterojunctions. This sensor can capture various degrees of stretching in human limb movements, including wrist bending, finger bending and elbow bending. Moreover, as the bending angle increases, the output electrical signal also strengthens. Furthermore, the sensor achieves a rapid response time of 48 ms (Fig. S15), which compares favorably with previously reported values ranging from 74 ms to 142.1 ms [64-66]. Fig. 6d illustrates the equivalent circuit of the wearable system. Mechanical stability and repeatability were evaluated by performing 1500 consecutive operating cycles (Fig. 6e). Comparison of cycles 300-320 and 1300-1320 showed negligible signal attenuation, confirming long-term durability. In conclusion, the BP/Bi integrated system balances self-powering, high-sensitivity sensing, and long-term stability, exhibiting significant potential for human motion monitoring and continuous, stable detection of human activity signals.

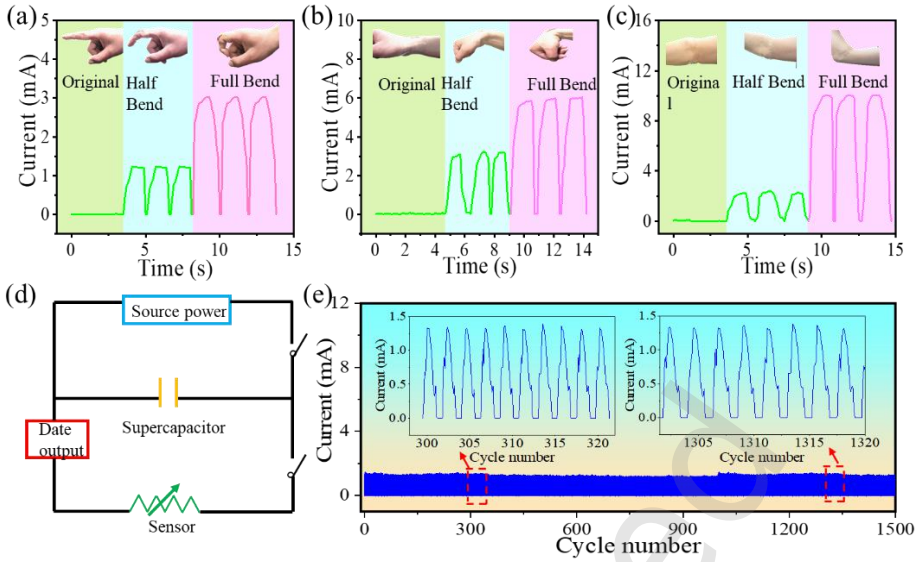

Fig. 6. Performance of the integrated BP/Bi (3:1) wearable sensing system. Real-time sensing signals recorded at the (a) finger, (b) wrist, and (c) elbow under different bending angles. (d) Equivalent circuit of the sensing system. (e) Signal stability during 1500 operational cycles (inset: magnified comparison of cycles 300 - 320 and 1300 - 1320).

4. Conclusions

This work reports the rational design of a synergistically coupled 2D BP/Bi heterojunction bifunctional electrode, enabling a monolithic flexible system integ rating MSC energy storage and piezoresistive sensing. Via liquid nitrogen-assist ed low-energy exfoliation and scalable mask-assisted filtration, phosphorene and bismuthene were assembled, with interfacial P-O-Bi covalent bonds addressing BP's intrinsic instability and low conductivity by suppressing restacking, sugge sts improved structural/electrochemical robustness, and accelerating ion/charge tr ansport. The optimized BP/Bi (3:1) MSC delivers 7.46 mF cm^{-2}, retains 92.1% capacitance after 30,000 cycles and maintains 70% of room-temperature capaci

tance at -30 °C. Leveraging graphene as a flexible current collector, the system achieves monolithic energy-sensing integration for conformal motion monitoring, with ultra-fast response (~48 ms) and negligible signal attenuation over 900 cycles. This integrated system shows promise for wearable electronics in extreme environments and can be further extended to multifunctional sensing platforms. More broadly, this study validates BP/Bi heterojunctions as a solution to BP's key drawbacks and provides a generalizable design paradigm for high-performance multifunctional integrated systems, offering new insights for next-generation flexible electronics in health monitoring, smart human-machine interaction, and extreme-environment exploration.

Data availability

Data will be made available on request.

Declaration of competing interest

The authors declare that they have no known competing financial interests or personal relationships that could have appeared to influence the work reported in this paper.

Acknowledgements

This work was supported by the National Natural Science Foundations of China (Grant No. 52202364, 52372284, 52275187), Natural Science Foundation of Henan (232300421135), Henan Central-Guided Local S&T Development Fund (Z20241471061), "Double First-Class" Initiative Cultivation Program of Safety and Energy Engineering at Henan Polytechnic University (AQ20250704). This project is also supported by the Support Program for Excellent Young Talents in Universities of Anhui Province (Grant No. 2022AH030134) and Excellent Young College Teacher Training Program of Anhui Provincial Department of Education (Grant No. YQZD2025090).

References

[1] Q. Tang, Y. Zhang, X. Zhu, Y. Wang, Z. Man, C. Yang, J. Xu, G. Wu, W. Lu, Hier archically Porous and Hetero‐Structured Black Phosphorus/$Ti_3C_2T_X$ MXene Aerogel Fiber for Wearable Supercapacitors with Implantable Capability, Adv. Funct. Mater. 3 4 (2024) 2410005. https://doi.org/10.1002/adfm.202410005.

[2] X. Chen, Z. Lou, X. Gao, L. Yin, S. Qin, M. Lin, F. Zhang, Y. Lu, S. Ding, R. Li u, S. Tang, S. Zhou, D.T. Dang, X. Yang, Z. Wu, Z. Zhang, H. Hu, X. Wang, Y. Z hu, Y. Xu, R. Sheng, J. Zhou, C. Lu, R. Wang, W. Yue, H. Huang, R.S. Wu, Y. Bi an, G. Park, J. Cao, X. Liu, D. Luo, G. Cauwenberghs, J. Wang, S. Xu, A noise-tol erant human–machine interface based on deep learning-enhanced wearable sensors, Na t. Sens. (2025). https://doi.org/10.1038/s44460-025-00001-3.

[3] T. Tan, X. Jiang, C. Wang, B. Yao, H. Zhang, 2D Material Optoelectronics for Infor mation Functional Device Applications: Status and Challenges, Adv. Sci. 7 (2020) 20 00058. https://doi.org/10.1002/advs.202000058.

[4] Z. Zheng, W. Wu, T. Yang, E. Wang, Z. Du, X. Hou, T. Liang, H. Wang, In situ re duced MXene/AuNPs composite toward enhanced charging/discharging and specific ca pacitance, J. Adv. Ceram. 10 (2021) 1061–1071. https://doi.org/10.1007/s40145-021-04 91-0.

[5] Q. Xia, R. Miao, W. Guo, M. Xia, L. Wang, Q. Hu, A. Zhou, Self-assembled Fe_3O_4 nanoparticles on V_2C MXene for enhanced supercapacitor and microwave absorption applications, J. Adv. Ceram. 14 (2025) 9221049. https://doi.org/10.26599/JAC.2025.92 21049.

[6] S. Park, H. Lee, Y.-J. Kim, P.S. Lee, Fully laser-patterned stretchable microsupercapa citors integrated with soft electronic circuit components, NPG Asia Mater. 10 (2018) 959–969. https://doi.org/10.1038/s41427-018-0080-z.

[7] J. Meng, Z. Tan, Y. Chen, W. Fan, C. Zhang, L. Li, T. Liu, Host‐Guest All‐in‐One Supercapacitors Enabled by 3D‐Printed Zwitterionic Gel Microlattices for Adva nced Energy Storage, Adv. Funct. Mater. (2025) e20575. https://doi.org/10.1002/adfm.2 02520575.

[8] D. Zhang, X. Gao, H. Liu, Z. Wu, X. Wang, A Multifunctional Conductive Binder Network Stabilizing Black Phosphorus Anodes for Long‐Cycle‐Life Lithium‐Ion Batteries, Adv. Energy Mater. (2025) e05146. https://doi.org/10.1002/aenm.202505146.

[9] J. Liu, Z. Xia, Y. Chen, D. Tao, Q. Zhang, Enhanced ionic conductivity of Ce-doped $Na_3Zr_2Si_2PO_{12}$ electrolyte for achieving superior performance of solid-state sodium b atteries, J. Adv. Ceram. 14 (2025) 9221023. https://doi.org/10.26599/JAC.2024.922102 3.

[10] Y. Liu, X. Chen, B. Mao, Y. Ying, L. Li, W. Shi, Black phosphorus quantum dots e nabled photo-assisted supercapacitor with boosted volumetric charge storage capability, J. Mater. Sci. Technol. 191 (2024) 80–88. https://doi.org/10.1016/j.jmst.2023.12.036.

[11] C. Hao, B. Yang, F. Wen, J. Xiang, L. Li, W. Wang, Z. Zeng, B. Xu, Z. Zhao, Z. Liu, Y. Tian, Flexible All‐Solid‐State Supercapacitors based on Liquid‐Exfoliated Black‐Phosphorus Nanoflakes, Adv. Mater. 28 (2016) 3194–3201. https://doi.org/10.1 002/adma.201505730.

[12] X. Wu, Y. Xu, Y. Hu, G. Wu, H. Cheng, Q. Yu, K. Zhang, W. Chen, S. Chen, Microfluidic-spinning construction of black-phosphorus-hybrid microfibres for non-woven fabrics toward a high energy density flexible supercapacitor, Nat. Commun. 9 (2018) 4573. https://doi.org/10.1038/s41467-018-06914-7.

[13] H. Xiao, Z.-S. Wu, L. Chen, F. Zhou, S. Zheng, W. Ren, H.-M. Cheng, X. Bao, One-Step Device Fabrication of Phosphorene and Graphene Interdigital Micro-Supercapacitors with High Energy Density, ACS Nano 11 (2017) 7284–7292. https://doi.org/10.1021/acsnano.7b03288.

[14] T. Akram, L. Arshad, T. Ahmed, A. Saleem, M. Ammar, A. Yusaf, Insight into two-dimensional black phosphorus: An emerging energy storage material, Mater. Sci. Eng. B 299 (2024) 117002. https://doi.org/10.1016/j.mseb.2023.117002.

[15] Z. Wu, Y. Lyu, Y. Zhang, R. Ding, B. Zheng, Z. Yang, S.P. Lau, X.H. Chen, J. Hao, Large-scale growth of few-layer two-dimensional black phosphorus, Nat. Mater. 20 (2021) 1203–1209. https://doi.org/10.1038/s41563-021-01001-7.

[16] H. Chen, X. Ge, Y. Wang, Q. Xu, Z. Li, X. Zhou, J. Hao, W. Hu, S. Li, X. Wang, Uniaxial Strain-Induced Tunable Mid-infrared Light Emission from Thin Film Black Phosphorus, J. Phys. Chem. Lett. 14 (2023) 2092–2098. https://doi.org/10.1021/acs.jpclett.3c00145.

[17] S.C. Kishore, S. Perumal, R. Atchudan, M. Alagan, A.K. Sundramoorthy, S. Ramalingam, D. Manoj, S. Sambasivam, A critical review on black phosphorus and its utilization in the diverse range of sensors, Sens. Actuators Phys. 377 (2024) 115719. https://doi.org/10.1016/j.sna.2024.115719.

[18] Y. Wang, Y. Zhou, Y. Wang, R. Zhang, J. Li, X. Li, Z. Zang, Conductometric room temperature ammonia sensors based on titanium dioxide nanoparticles decorated thin black phosphorus nanosheets, Sens. Actuators B Chem. 349 (2021) 130770. https://doi.org/10.1016/j.snb.2021.130770.

[19] Z. Wu, L. Liang, S. Zhu, Y. Guo, Y. Yao, Y. Yang, S. Gu, Z. Zhou, High Sensitivity of Ammonia Sensor through 2D Black Phosphorus/Polyaniline Nanocomposite, Nanomaterials 11 (2021) 3026. https://doi.org/10.3390/nano11113026.

[20] Y. Wang, Y. Zhou, H. Ren, Y. Wang, X. Zhu, Y. Guo, X. Li, Room-Temperature and Humidity-Resistant Trace Nitrogen Dioxide Sensing of Few-Layer Black Phosphorus Nanosheet by Incorporating Zinc Oxide Nanowire, Anal. Chem. 92 (2020) 11007–11017. https://doi.org/10.1021/acs.analchem.9b05623.

[21] T. Chen, Z. Cheng, Q. Tian, J. Wang, X. Yu, D. Ho, Nitrogen Dioxide Gas Sensor Based on Liquid-Phase-Exfoliated Black Phosphorus Nanosheets, ACS Appl. Nano Mater. 3 (2020) 6440–6447. https://doi.org/10.1021/acsanm.0c00922.

[22] Y. Chen, R. Ren, H. Pu, J. Chang, S. Mao, J. Chen, Field-effect transistor biosensors with two-dimensional black phosphorus nanosheets, Biosens. Bioelectron. 89 (2017) 505–510. https://doi.org/10.1016/j.bios.2016.03.059.

[23] Y. Cai, D. Chen, Y. Chen, T. Li, L. Wang, J. Jiang, Z. Guo, N. Jaffrezic-Renault, Z. Zhang, S. Huang, An electrochemical biosensor based on graphene intercalated functionalized black phosphorus/gold nanoparticles nanocomposites for the detection of bacterial enzyme, Microchem. J. 193 (2023) 109255. https://doi.org/10.1016/j.microc.2023.109255.

[24] X. Chen, Q. Li, T. Yuan, M. Ma, Z. Ye, X. Wei, X. Fang, S. Mao, Highly Specific Antibiotic Detection on Water-Stable Black Phosphorus Field-Effect Transistors, ACS Sens. 8 (2023) 858–866. https://doi.org/10.1021/acssensors.2c02562.

[25] H. Besbes, F. Ouerghui, M. Omri, S. Haxha, F. AbdelMalek, Label-free microring biosensor with enhanced sensitivity for detection of influenza A viruses H1N1 and H_9N_2, Alex. Eng. J. 77 (2023) 255–264. https://doi.org/10.1016/j.aej.2023.06.045.

[26] H. Kim, S.Z. Uddin, D.-H. Lien, M. Yeh, N.S. Azar, S. Balendhran, T. Kim, N. Gupta, Y. Rho, C.P. Grigoropoulos, K.B. Crozier, A. Javey, Actively variable-spectrum optoelectronics with black phosphorus, Nature 596 (2021) 232–237. https://doi.org/10.1038/s41586-021-03701-1.

[27] J. Chen, G. Ma, X. Wang, T. Song, Y. Zhu, S. Jia, X. Zhang, Y. Zhao, J. Chen, B. Yang, Y. Li, Multifunctional black phosphorus pressure sensors with bending angle monitoring and direction recognition characteristics, Nanoscale 16 (2024) 5999–6009. https://doi.org/10.1039/D3NR05372E.

[28] Y. Zhang, L. Wang, L. Zhao, K. Wang, Y. Zheng, Z. Yuan, D. Wang, X. Fu, G. Shen, W. Han, Flexible Self‐Powered Integrated Sensing System with 3D Periodic Ordered Black Phosphorus@MXene Thin‐Films, Adv. Mater. 33 (2021) 2007890. https://doi.org/10.1002/adma.202007890.

[29] Z.-C. Luo, M. Liu, Z.-N. Guo, X.-F. Jiang, A.-P. Luo, C.-J. Zhao, X.-F. Yu, W.-C. Xu, H. Zhang, Microfiber-based few-layer black phosphorus saturable absorber for ultra-fast fiber laser, Opt. Express 23 (2015) 20030. https://doi.org/10.1364/OE.23.020030.

[30] X. Zhu, J. Yang, X. She, Y. Song, J. Qian, Y. Wang, H. Xu, H. Li, Q. Yan, Rapid synthesis of ultrathin 2D materials through liquid-nitrogen and microwave treatments, J. Mater. Chem. A 7 (2019) 5209–5213. https://doi.org/10.1039/C8TA11497H.

[31] F. Zhou, L. Ouyang, M. Zeng, J. Liu, H. Wang, H. Shao, M. Zhu, Growth mechanism of black phosphorus synthesized by different ball milling techniques, J. Alloys Compd. 784 (2019) 339–346. https://doi.org/10.1016/j.jallcom.2019.01.023.

[32] B. Yang, X. Li, Y. Cheng, S. Duan, B. Zhao, W. Yi, C. Wang, H. Sun, Z. Wang, D. Gu, S. Chen, X. Liu, Liquid phase exfoliation of bismuth nanosheets for flexible all-solid-state supercapacitors with high energy density, J. Mater. Chem. C 8 (2020) 12314–12322. https://doi.org/10.1039/D0TC03134H.

[33] H. Wang, C. Tang, B. Sun, J. Liu, Y. Xia, W. Li, C. Jiang, D. He, X. Xiao, In-situ structural evolution of Bi_2O_3 nanoparticle catalysts for CO_2 electroreduction, Int. J. Extreme Manuf. 4 (2022) 035002. https://doi.org/10.1088/2631-7990/ac7a6e.

[34] P. Yasaei, A. Behranginia, T. Foroozan, M. Asadi, K. Kim, F. Khalili-Araghi, A. Salehi-Khojin, Stable and Selective Humidity Sensing Using Stacked Black Phosphorus Flakes, ACS Nano 9 (2015) 9898–9905. https://doi.org/10.1021/acsnano.5b03325.

[35] J. Kang, J.D. Wood, S.A. Wells, J.-H. Lee, X. Liu, K.-S. Chen, M.C. Hersam, Solvent Exfoliation of Electronic-Grade, Two-Dimensional Black Phosphorus, ACS Nano 9 (2015) 3596–3604. https://doi.org/10.1021/acsnano.5b01143.

[36] J. Zhou, J. Chen, M. Chen, J. Wang, X. Liu, B. Wei, Z. Wang, J. Li, L. Gu, Q. Zhang, H. Wang, L. Guo, Few‐Layer Bismuthene with Anisotropic Expansion for High‐Areal‐Capacity Sodium‐Ion Batteries, Adv. Mater. 31 (2019) 1807874. https://d

oi.org/10.1002/adma.201807874.

[37] J. Yang, J. Xian, Q. Liu, Y. Sun, G. Li, Bi nanoparticles in situ encapsulated by car bon film as high-performance anode materials for Li-ion batteries, J. Energy Chem. 69 (2022) 524–530. https://doi.org/10.1016/j.jechem.2022.01.026.

[38] Y. Peng, Y. Wang, Z. Wang, G. Shao, B. Hou, Decoupling Dual Regulatory Roles a nd Mechanisms of Bismuth in Low‐Carbon‐Content Sn Anode for Fast and Stable Sodium Storage, Adv. Funct. Mater. (2025) e13942. https://doi.org/10.1002/adfm.2025 13942.

[39] M. Baibarac, T. Burlanescu, M. Stroe, I. Smaranda, C. Negrila, The Photoluminescen ce and Vibrational Properties of Black Phosphorous Sheets Chemically/Electrochemica lly Functionalized in the Presence of Diphenylamine, Polymers 14 (2022) 4479. https: //doi.org/10.3390/polym14214479.

[40] H. Doweidar, Y.B. Saddeek, FTIR and ultrasonic investigations on modified bismuth borate glasses, J. Non-Cryst. Solids 355 (2009) 348–354. https://doi.org/10.1016/j.jnon crysol.2008.12.008.

[41] X. Xin, Y. Xu, H. Wuliji, F. Sun, Q. Liu, Z. Wang, T. Wei, X. Zhao, X. Song, L. Gao, Covalently Assembled Black Phosphorus/Conductive C_3N_4 Hybrid Material for F lexible Supercapacitors Exhibiting a Superlong 30,000 Cycle Durability, ACS Nano 1 7 (2023) 657–667. https://doi.org/10.1021/acsnano.2c09970.

[42] K.L. Kuntz, R.A. Wells, J. Hu, T. Yang, B. Dong, H. Guo, A.H. Woomer, D.L. Druf fel, A. Alabanza, D. Tománek, S.C. Warren, Control of Surface and Edge Oxidation on Phosphorene, ACS Appl. Mater. Interfaces 9 (2017) 9126–9135. https://doi.org/10.1 021/acsami.6b16111.

[43] Q. Zhou, Q. Chen, Y. Tong, J. Wang, Light‐Induced Ambient Degradation of Few ‐Layer Black Phosphorus: Mechanism and Protection, Angew. Chem. Int. Ed. 55 (2 016) 11437–11441. https://doi.org/10.1002/anie.201605168.

[44] C. Wang, M. Chen, Z.H. Li, M. Zhou, Formation and Infrared Spectroscopic Charact erization of Three Oxygen-Rich BiO_4 Isomers in Solid Argon, J. Phys. Chem. A 117 (2013) 11217–11224. https://doi.org/10.1021/jp406126c.

[45] Q. Liao, W. Hou, K. Liao, L. Chen, Y. Song, G. Gao, L. Qin, Solid-phase sintering and vapor-liquid-solid growth of BP@MgO quantum dot crystals with a high piezoe lectric response, J. Adv. Ceram. 11 (2022) 1725–1734. https://doi.org/10.1007/s40145-022-0643-x.

[46] Y. Wang, K. Chen, H. Hao, G. Yu, B. Zeng, H. Wang, F. Zhang, L. Wu, J. Li, S. Xiao, J. He, Y. Zhang, H. Zhang, Engineering ultrafast charge transfer in a bismuthe ne/perovskite nanohybrid, Nanoscale 11 (2019) 2637–2643. https://doi.org/10.1039/C9N R00058E.

[47] S.G. G S, N. Abraham, H. R S, R. S, T.S. Xavier, Optimization studies on output st abilization time and graphene oxide concentration in graphene-based flexible micro-su percapacitor, Nanotechnology 36 (2025) 085401. https://doi.org/10.1088/1361-6528/ad9 83a.

[48] W. Wang, L. Xu, L. Zhang, A. Zhang, J. Zhang, Self‐Powered Integrated Sensing System with In‐Plane Micro‐Supercapacitors for Wearable Electronics, (2023).

[49] Y.-Y. Peng, B. Akuzum, N. Kurra, M.-Q. Zhao, M. Alhabeb, B. Anasori, E.C. Kumb

ur, H.N. Alshareef, M.-D. Ger, Y. Gogotsi, All-MXene (2D titanium carbide) solid-sta te microsupercapacitors for on-chip energy storage, Energy Environ. Sci. 9 (2016) 28 47–2854. https://doi.org/10.1039/C6EE01717G.

[50] S.A. Adewinbi, R.A. Busari, L.O. Animasahun, E. Omotoso, B.A. Taleatu, Effective pseudocapacitive performance of binder free transparent α-V_2O_5 thin film electrode: E lectrochemical and some surface probing, Phys. B Condens. Matter 621 (2021) 41326 0. https://doi.org/10.1016/j.physb.2021.413260.

[51] W. Tian, Y. Li, J. Zhou, T. Wang, R. Zhang, J. Cao, M. Luo, N. Li, N. Zhang, H. Gong, J. Zhang, L. Xie, B. Kong, Implantable and Biodegradable Micro-Supercapacit or Based on a Superassembled Three-Dimensional Network Zn@PPy Hybrid Electrod e, ACS Appl. Mater. Interfaces 13 (2021) 8285–8293. https://doi.org/10.1021/acsami.0c 19740.

[52] S. Xu, Y. Dall'Agnese, G. Wei, C. Zhang, Y. Gogotsi, W. Han, Screen-printable micr oscale hybrid device based on MXene and layered double hydroxide electrodes for p owering force sensors, Nano Energy 50 (2018) 479–488. https://doi.org/10.1016/j.nano en.2018.05.064.

[53] C. (John) Zhang, M.P. Kremer, A. Seral‐Ascaso, S. Park, N. McEvoy, B. Anasori, Y. Gogotsi, V. Nicolosi, Stamping of Flexible, Coplanar Micro‐Supercapacitors Usin g MXene Inks, Adv. Funct. Mater. 28 (2018) 1705506. https://doi.org/10.1002/adfm.20 1705506.

[54] T. Huang, B. Gao, S. Zhao, H. Zhang, X. Li, X. Luo, M. Cao, C. Zhang, S. Luo, Y. Yue, Y. Ma, Y. Gao, All-MXenes zinc ion hybrid micro-supercapacitor with wide voltage window based on V_2CT_x cathode and $Ti_3C_2T_x$ anode, Nano Energy 111 (2023) 108383. https://doi.org/10.1016/j.nanoen.2023.108383.

[55] T. Wang, W. Yu, D. Wu, W. Zhao, M. Wang, J. Xu, J. Zhang, Biomass‐Derived In ks with Tailored Pteridine Derivatives for Sustainable Printed Micro‐Supercapacitors, Adv. Funct. Mater. 33 (2023) 2301896. https://doi.org/10.1002/adfm.202301896.

[56] X. Wang, W. Chen, X. Shi, P. Das, S. Zheng, J. Qin, C. Sun, Z. Wu, Microfluidics ‐Assisted Fabrication of All‐Flexible Substrate‐Free Micro‐Supercapacitors with Customizable Configuration and High Performance, Adv. Energy Mater. 13 (2023) 22 03535. https://doi.org/10.1002/aenm.202203535.

[57] J. Chen, W. Zhao, Y. Gao, F. Bu, P. Wu, Y. Xiang, J. Wang, X. Liu, C. Guan, Sing le-layer MoS_2/graphene-based stable on-chip Zn-ion microbattery for monolithically int egrated electronics, Sci. Bull. 70 (2025) 508–517. https://doi.org/10.1016/j.scib.2024.11. 023.

[58] S. Deshmukh, K. Ghosh, M. Pykal, M. Otyepka, M. Pumera, Laser-Induced MXene-Functionalized Graphene Nanoarchitectonics-Based Microsupercapacitor for Health Mo nitoring Application, ACS Nano 17 (2023) 20537–20550. https://doi.org/10.1021/acsna no.3c07319.

[59] A.S. Keefe, S. Buteau, I.G. Hill, J.R. Dahn, Temperature Dependent EIS Studies Sep arating Charge Transfer Impedance from Contact Impedance in Lithium-Ion Symmetri c Cells, J. Electrochem. Soc. 166 (2019) A3272–A3279. https://doi.org/10.1149/2.0541 914jes.

[60] X. Jiang, J. Jia, Y. Zhu, J. Li, H. Jia, C. Liu, G. Zhao, L. Yu, G. Zhu, Beyond con

ventional limits: Advancements and insights in broadening operating temperature ranges of supercapacitors, Energy Storage Mater. 70 (2024) 103462. https://doi.org/10.1016/j.ensm.2024.103462.

[61] X. Wang, H.-J. Kim, Ultra-stretchable dual-network ionic hydrogel strain sensor with moistening and anti-freezing ability, Prog. Org. Coat. 166 (2022) 106784. https://doi.org/10.1016/j.porgcoat.2022.106784.

[62] Y. Liu, H. Li, X. Wang, T. Lv, K. Dong, Z. Chen, Y. Yang, S. Cao, T. Chen, Flexible supercapacitors with high capacitance retention at temperatures from −20 to 100 °C based on DMSO-doped polymer hydrogel electrolytes, J. Mater. Chem. A 9 (2021) 12051–12059. https://doi.org/10.1039/D1TA02397G.

[63] X. Hou, Q. Zhang, L. Wang, G. Gao, W. Lü, Low-Temperature-Resistant Flexible Solid Supercapacitors Based on Organohydrogel Electrolytes and Microvoid-Incorporated Reduced Graphene Oxide Electrodes, ACS Appl. Mater. Interfaces 13 (2021) 12432–12441. https://doi.org/10.1021/acsami.0c18741.

[64] T. Xu, Q. Song, K. Liu, H. Liu, J. Pan, W. Liu, L. Dai, M. Zhang, Y. Wang, C. Si, H. Du, K. Zhang, Nanocellulose-Assisted Construction of Multifunctional MXene-Based Aerogels with Engineering Biomimetic Texture for Pressure Sensor and Compressible Electrode, Nano-Micro Lett. 15 (2023) 98. https://doi.org/10.1007/s40820-023-01073-x.

[65] Pu, Y. Gao, Z. Geng, Y. Zhang, Q. Cao, J. Yang, X. Zhao, Y. Wang, J. Wang, C. Guan, Grafted MXene Assisted Bifunctional Hydrogel for Stable and Highly Sensitive Self‐Powered Fibrous System, Adv. Funct. Mater. 34 (2024) 2304453. https://doi.org/10.1002/adfm.202304453.

[66] J. Pu, Q. Cao, Y. Gao, Q. Wang, Z. Geng, L. Cao, F. Bu, N. Yang, C. Guan, Liquid Metal‐Based Stable and Stretchable Zn‐Ion Battery for Electronic Textiles, Adv. Mater. 36 (2024) 2305812. https://doi.org/10.1002/adma.202305812.

Electronic Supplementary Material

Interface-stabilized phosphorene/bismuthene heterostructures for freeze-tolerant micro-supercapacitors and integrated sensing

Yukai Chang[1,*], Chenfang Lou[1], Jin Jia[2], Huilan Zhao[1], Penghui Li[3,*], Yingjie Huo[4], Libo Wang[1], Qianku Hu[1], Yuanyuan Zhu[2,*], and Aiguo Zhou[1,*]

[1] School of Materials Science and Engineering, Henan Polytechnic University, Jiaozuo 454003, China

[2] Key Laboratory of Spin Electron and Nanomaterials of Anhui Higher Education Institutes, Suzhou University, Suzhou 234000, China

[3] Center for High Pressure Science (CHiPS), State Key Laboratory of Metastable Materials Science and Technology, Yanshan University, Qinhuangdao 066004, China

[4] School of Physical Science and Technology, Tangshan Normal University, Tangshan 063000, China

*Address correspondence to Yukai Chang, yukaichang12345@hpu.edu.cn; Penghui Li, ysulph@163.com; Yuanyuan Zhu, zhuyy@ahszu.edu.cn; Aiguo Zhou, zhouag@hpu.edu.cn

Supporting information to https://doi.org/10.26599/NR.2026.94908756

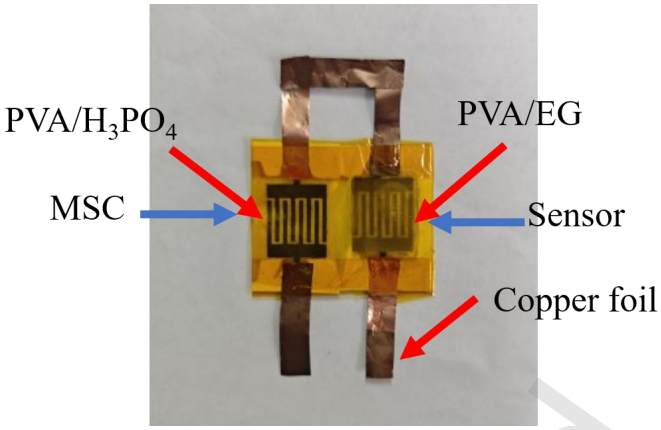

Fig. S1 Schematic diagram of black phosphorus/bismuth capacitor-sensing integration.

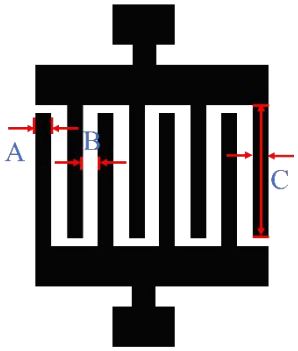

A (mm)	1
B (mm)	1
C (mm)	10

Fig. S2 Schematic illustration of key structural parameters of the electrode template. A: wideth of electrode. B: interspace. C: length of electrode

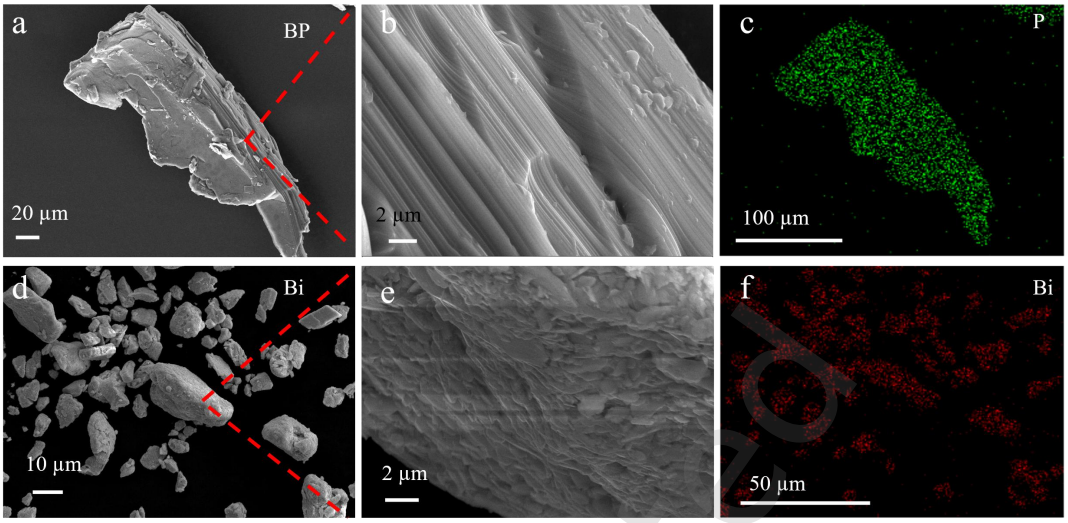

Fig. S3 Morphological and elemental characterization of bulk BP and Bi powder. (a,b) SEM images and (c) EDS pattern of bulk BP. (d,e) SEM images and (f) EDS pattern of Bi powder.

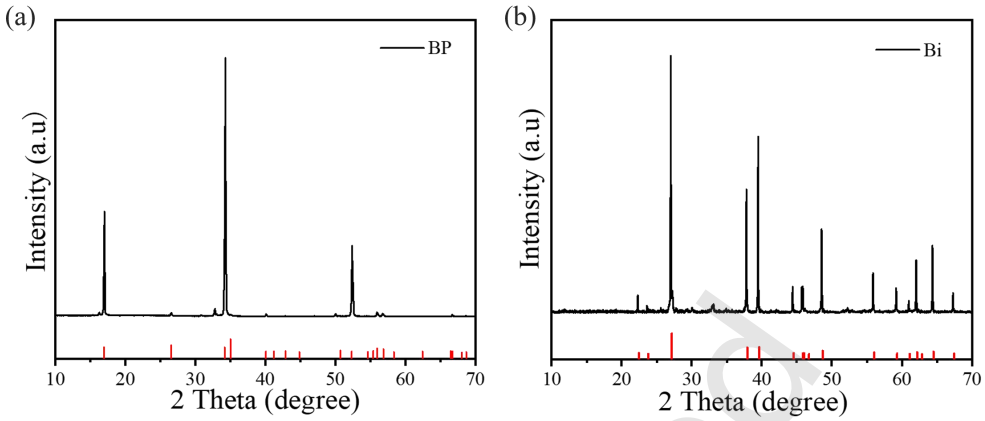

Fig. S4 X-ray diffraction (XRD) patterns of the raw materials used for electrode fabrication. (a) XRD pattern of bulk black phosphorus (BP), showing characteristic diffraction peaks corresponding to its orthorhombic crystal structure. The sharp and well-defined peaks indicate high crystallinity of the pristine BP. (b) XRD pattern of commercial Bi powder, with all diffraction peaks indexed to the rhombohedral phase of metallic bismuth. The absence of additional peaks confirms the high purity of the Bi precursor.

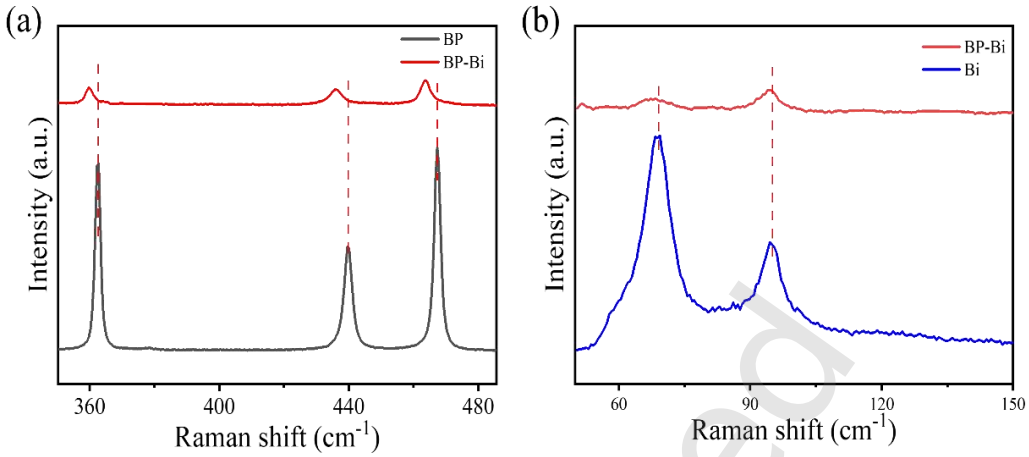

Fig. S5 Figure X. Raman spectra of the BP/Bi heterojunction electrode (BP:Bi = 3:1). (a) Comparison between BP/Bi and pristine BP/Bi showing shifted characteristic peaks of black phosphorus. (b) Local magnified comparison between BP/Bi and pure Bi in the low wavenumber region.

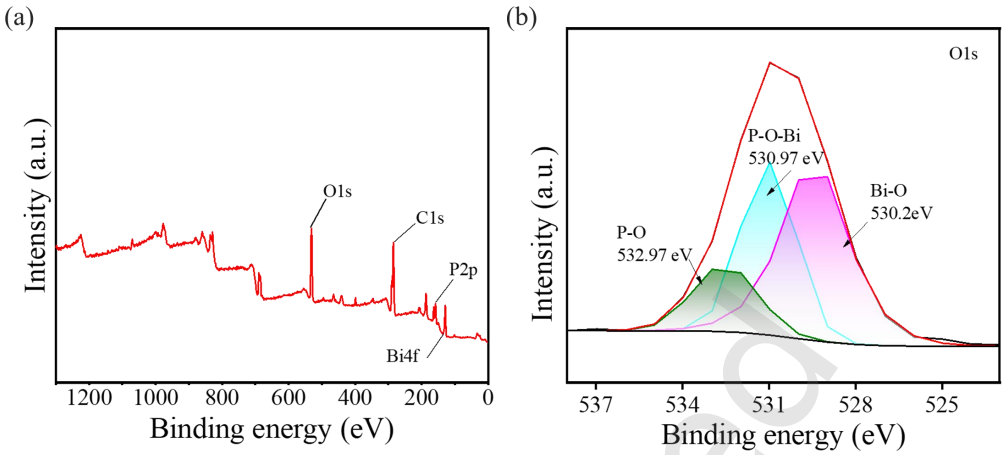

Fig. S6 (a) X-ray photoelectron spectroscopy (XPS) survey spectrum of the BP/Bi electrode (BP: Bi mass ratio of 3:1), which confirmed the presence of four elements: P, Bi, C, and O, and no impurities were detected. (b) High-resolution O 1s spectrum, which can be decomposed into multiple components corresponding to different chemical states.

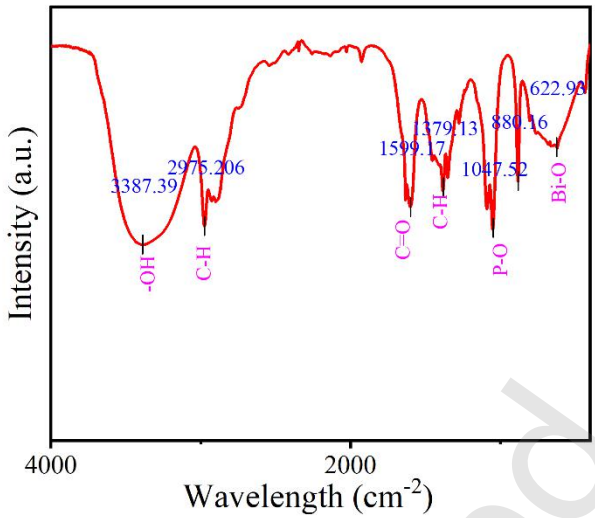

Fig. S7 FTIR spectrum of the BP/Bi heterojunction. The absorption bands at 1047 cm^{-1} and 623 cm^{-1} correspond to P-O and Bi-O vibrations, respectively, indicating interfacial interaction between BP and Bi.

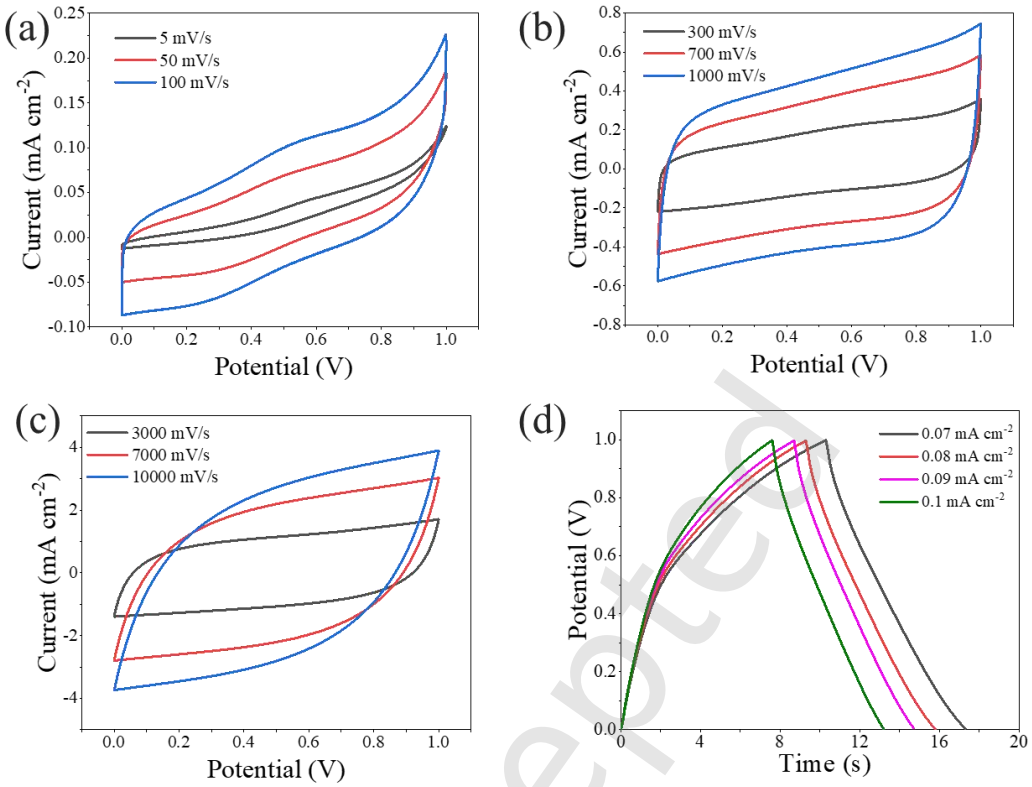

Fig. S8 The electrochemical performance of the pure BP MSCs. (a-c) CV curves at 5-10,000 mV s^{-1}. (d) GCD profiles at 0.07-0.1 mA cm^{-2}.

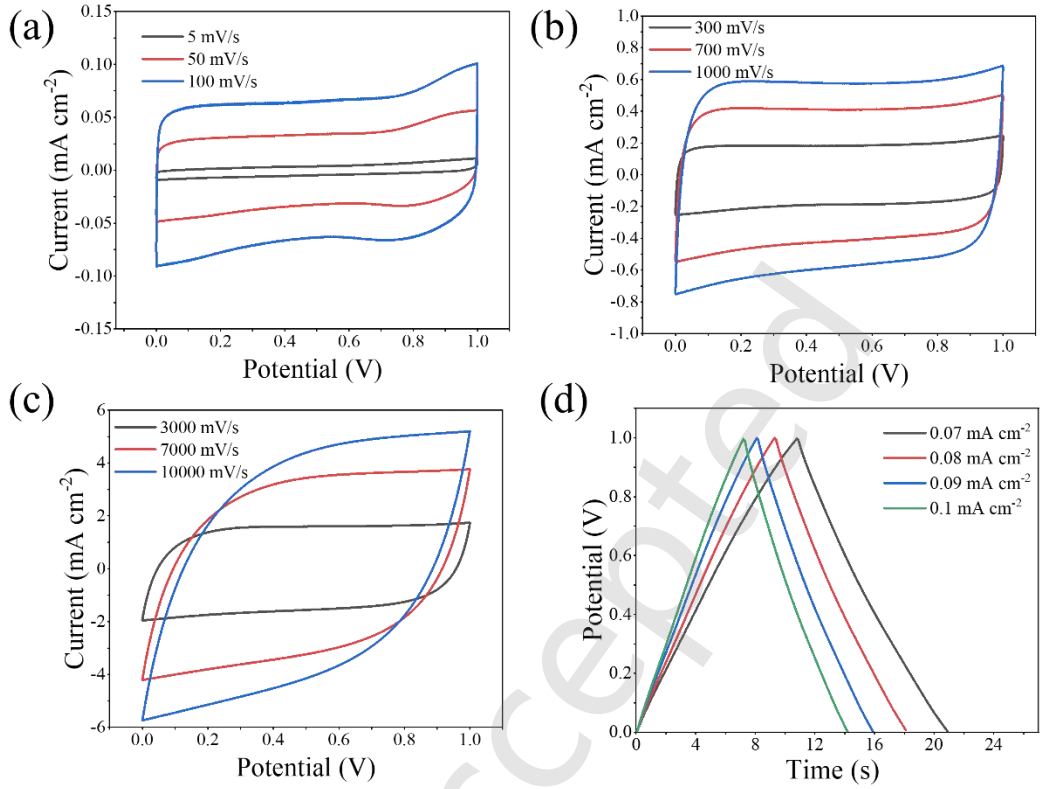

Fig. S9 The electrochemical performance of the pure bismuth MSCs. (a-c) CV curves at 5-10,000 mV s^{-1}. (d) GCD profiles at 0.07-0.1 mA cm^{-2}

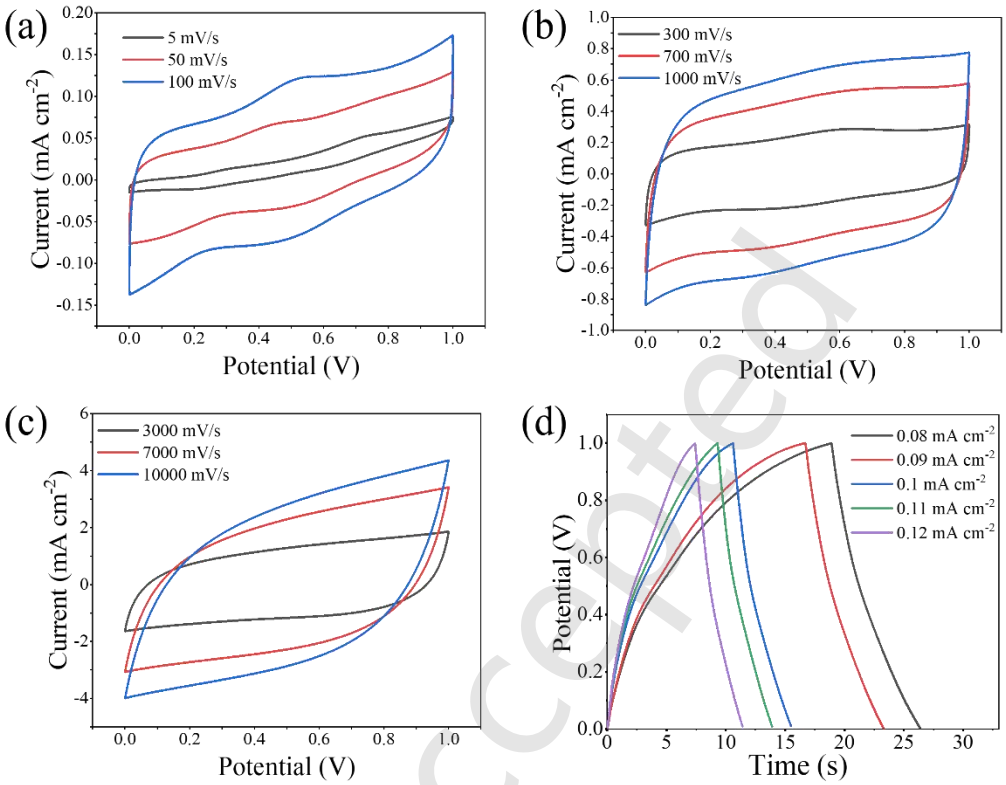

Fig. S10 The electrochemical performance of the BP/Bi 1:1 MSCs. (a-c) CV curves at 5-10,000 mV s^{-1}. (d) GCD profiles at 0.08-0.12 mA cm^{-2}.

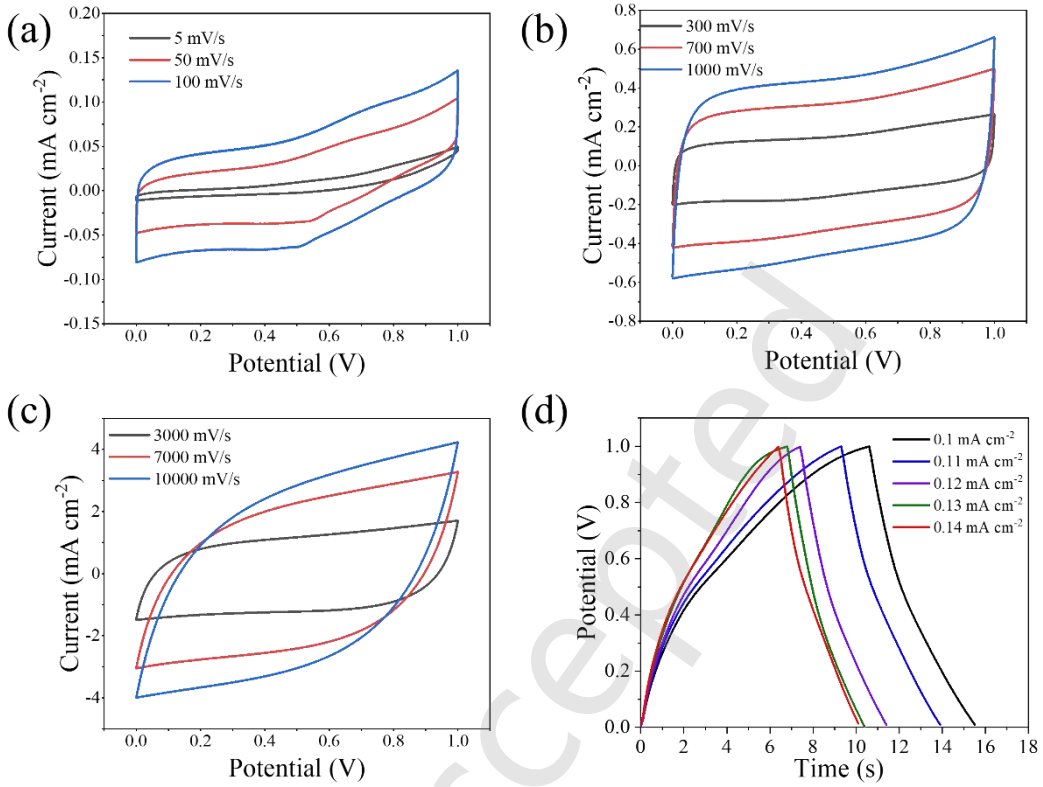

Fig. S11 Electrochemical performance of the BP/Bi 1:3 MSCs. (a-c) CV curves at 5-10,000 mV s^{-1}. (d) GCD profiles at 0.1-0.14 mA cm^{-2}.

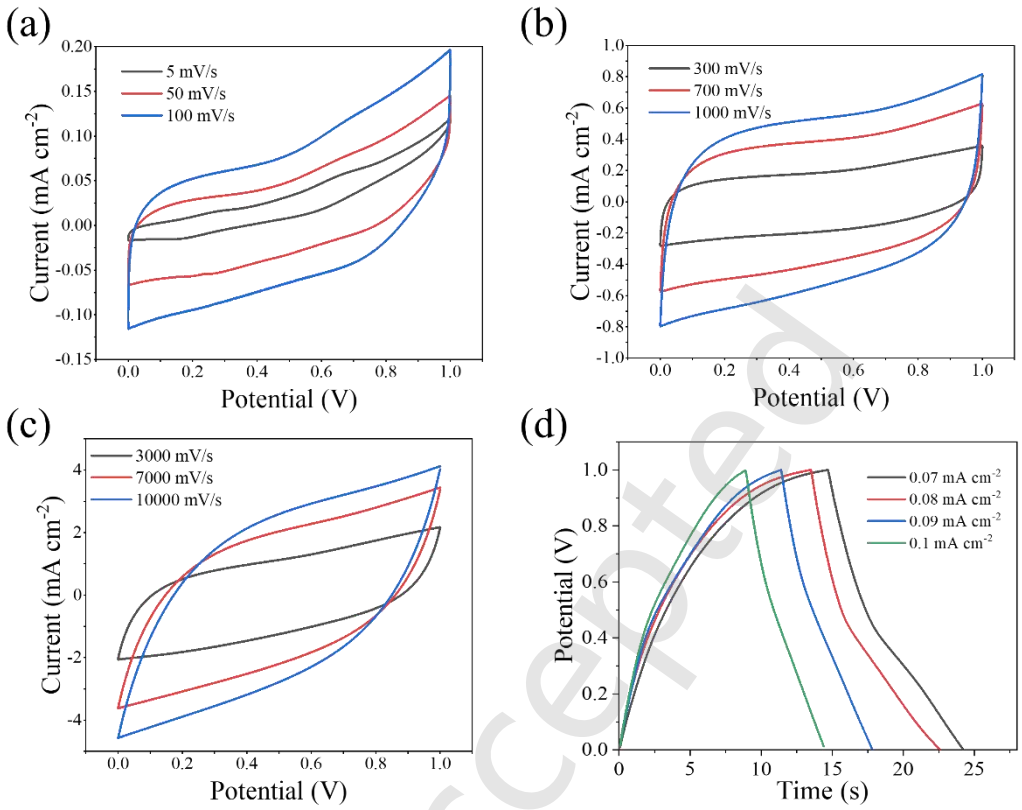

Fig. S12 Electrochemical performance of the BP/Bi 5:1 MSCs. (a-c) CV at 5-10,000 mV s^{-1}. (d) Constant current charge-discharge profiles at 0.07-0.1 mA cm^{-2}.

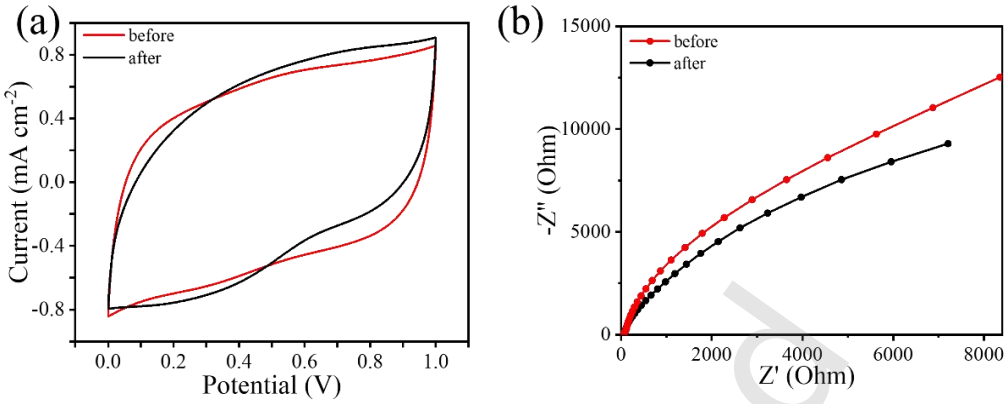

Fig. S13 Comparison of the electrochemical performance of BP/Bi 3:1 MSCs before and after 30,000 cycles: (a) CV curves and (b) EIS plots.

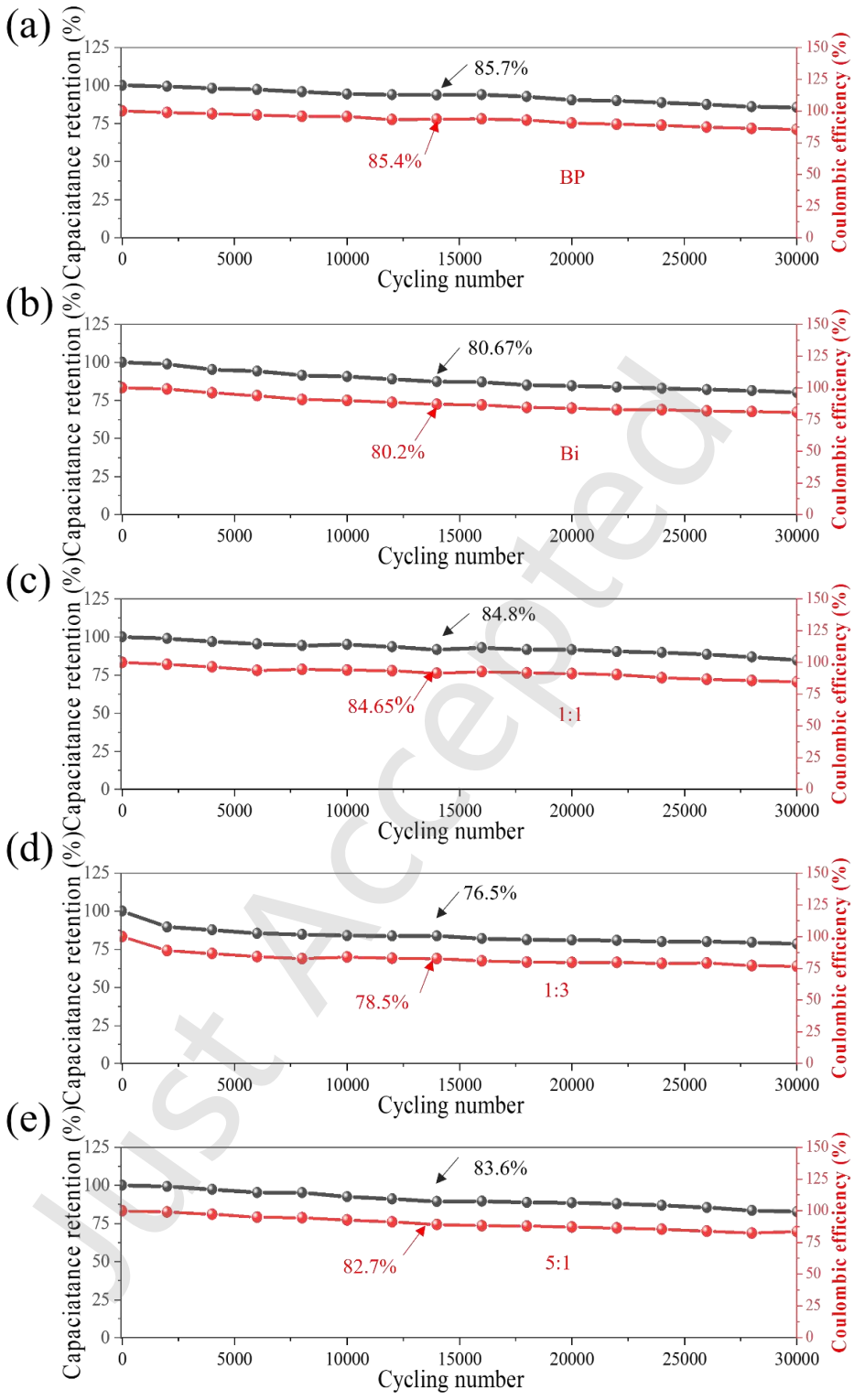

Fig. S14 Cycling stability of MSCs based on different electrode materials: (a) pure BP, (b) pure Bi, and BP/Bi composites with mass ratios of (c) 1:1, (d) 1:3, and (e) 1:5. Data were collected over 30,000 cycles.

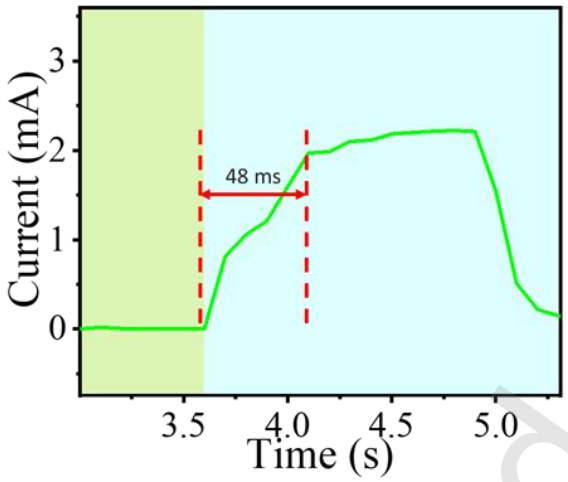

Fig. S15. Transient response curve of the BP/Bi (3:1) integrated pressure sensor. The plot shows the instantaneous current change upon rapid application and release of pressure, demonstrating a fast response time of approximately 48 ms .

Table S1 Comparison of the electrochemical performance of the BP/Bi 3:1 MSC with previously reported MSCs

Type	Electrolyte	C_A (mF cm^{-2})	C_V (mF cm^{-3})	Cycles	Cycling life	References
Co/rGO -MSCs	PVA/H_3PO_4	-	2.27	10000	70%	[1]
WS_2-MSCs	PVA-LiCl	0.93	-	10000	82%	[2]
PG-MSCs	Ionic liquid	9.8	-	2000	89.5%	[3]
BP-ASSP	PVA/H_3PO_4	-	13.75	30000	71.8%	[4]
SnP_3/CNT- FSCs	PVA/H_3PO_4	-	29.4	20000	88%	[5]
LIG-MSCs	PVA/H_2SO_4	1.66	-	10000	96%	[6]
Paper CO_2 laser	PVA/H_2SO_4	4.6	-	10000	85%	[7]
Cork/H_3BO_3 UV laser	PVA/H_2SO_4	4.67	-	10000	86%	[8]
graphene-based MSCs	PVA/H_2SO_4	9.15	-	10000	91.6%	[9]
Thin-film MSCs	H_2SO_4	18.44	-	7000	97%	[10]
BP/Bi MSCs	PVA/H_3PO_4	7.6	-	30000	92.1%	**This work**

C_A: Area capacitance; C_V: Volume capacitance; MSCs: Micro-supercapacitors; ASSP: All-solid-state supercapacitors; LIG: Laser-induced graphene; BP: Black phosphorus; PG: Phosphorene graphene; PVA: Polyvinyl alcohol.

References

[1] S.H. Lee, J. Lee, J. Jung, A.R. Cho, J.R. Jeong, C. Dang Van, J. Nah, M.H. Lee, Enhanced Electrochemical Performance of Micro-Supercapacitors Via Laser-Scribed Cobalt /Reduced Graphene Oxide Hybrids, ACS Appl. Mater. Interfaces 13 (2021) 18821–18828. https://doi.org/10.1021/acsami.1c02102.

[2] X. Zuo, K. Chang, J. Zhao, Z. Xie, H. Tang, B. Li, Z. Chang, Bubble-template-assisted synthesis of hollow fullerene-like MoS_2 nanocages as a lithium ion battery anode material, J. Mater. Chem. A 4 (2016) 51–58. https://doi.org/10.1039/C5TA06869J.

[3] H. Xiao, Z.-S. Wu, L. Chen, F. Zhou, S. Zheng, W. Ren, H.-M. Cheng, X. Bao, One-Step Device Fabrication of Phosphorene and Graphene Interdigital Micro-Supercapacitors with High Energy Density, ACS Nano 11 (2017) 7284–7292. https://doi.org/10.1021/acsnano.7b03288.

[4] C. Hao, B. Yang, F. Wen, J. Xiang, L. Li, W. Wang, Z. Zeng, B. Xu, Z. Zhao, Z. Liu, Y. Tian, Flexible All‐Solid‐State Supercapacitors based on Liquid‐Exfoliated Black‐Phosphorus Nanoflakes, Advanced Materials 28 (2016) 3194–3201. https://doi.org/10.1002/adma.201505730.

[5] M. Yan, B. Yang, X. Sun, Z. Wang, X. Jiang, W. Yi, H. Sun, R. Yang, H. Ding, D. Yue, K. Zhai, Y. Li, X. Chen, Y. Zhang, X. Liu, High-Quality 2D SnP_3 Nanosheets: Novel Flexible Electrode for Energy Storage Device Application with Wide Temperature Adaptivity, ACS Materials Lett. 6 (2024) 194–202. https://doi.org/10.1021/acsmaterialslett.3c01438.

[6] R. Correia, J. Deuermeier, M.R. Correia, J. Vaz Pinto, J. Coelho, E. Fortunato, R. Martins, Biocompatible Parylene-C Laser-Induced Graphene Electrodes for Microsupercapacitor Applications, ACS Appl. Mater. Interfaces 14 (2022) 46427–46438. https://doi.org/10.1021/acsami.2c09667.

[7] J. Coelho, R.F. Correia, S. Silvestre, T. Pinheiro, A.C. Marques, M.R.P. Correia, J.V. Pinto, E. Fortunato, R. Martins, Paper-based laser-induced graphene for sustainable and flexible microsupercapacitor applications, Microchim Acta 190 (2023) 40. https://doi.org/10.1007/s00604-022-05610-0.

[8] A. Imbrogno, J. Islam, C. Santillo, R. Castaldo, L. Sygellou, C. Larrigy, R. Murray, E. Vaughan, Md.K. Hoque, A.J. Quinn, D. Iacopino, Laser-Induced Graphene Supercapacitors by Direct Laser Writing of Cork Natural Substrates, ACS Appl. Electron. Mater. 4 (2022) 1541–1551. https://doi.org/10.1021/acsaelm.1c01202.

[9] Y. Wang, X. Zhang, Y. Zhu, X. Li, Z. Shen, Planar Micro-Supercapacitors with High Power Density Screen-Printed by Aqueous Graphene Conductive Ink, Materials 17 (2024) 4021. https://doi.org/10.3390/ma17164021.

[10] Z. Chen, C. Yan, Q. Dang, Y. Wang, Y. Xu, X. Deng, High-performance planar micro-supercapacitor arrays for integrated photo-detecting systems, Sci. China Mater. 67 (2024) 2169–2181. https://doi.org/10.1007/s40843-023-2877-x.